Incompressible Multiphase flow and Encapsulation simulations using the moment of fluid method [1]

Guibo Li[a], Yongsheng Lian[b], Yisen Guo[c], Matthew Jemison[d], Mark Sussman[e], Trevor Helms[f], Marco Arienti[g]

[a]*Mechanical Engineering, University of Louisville, Louisville, KY, U.S.A*
[b]*Mechanical Engineering, University of Louisville, Louisville, KY, U.S.A*
[c]*Mechanical Engineering, University of Louisville, Louisville, KY, U.S.A*
[d]*Mathematics, Florida State University, Tallahassee, FL, U.S.A*
[e]*Mathematics, Florida State University, Tallahassee, FL, U.S.A*
[f]*Mathematics, Florida State University, Tallahassee, FL, U.S.A*
[g]*Sandia National Labs, Livermore, CA, U.S.A*

Abstract

A moment of fluid method is presented for computing solutions to incompressible multiphase flows in which the number of materials can be greater than two. In this work, the multimaterial moment-of-fluid interface representation technique is applied to simulating surface tension effects at points where three materials meet. The advection terms are solved using a directionally split cell integrated semi-Lagrangian algorithm and the projection method is used to evaluate the pressure gradient force term. The underlying computational grid is a dynamic block structured adaptive grid. The new method is applied to multiphase problems illustrating contact line dynamics, triple junctions, and encapsulation in order to demonstrate its capabilities. Examples are given in 2D, 3D axisymmetric (R-Z), and 3D (X-Y-Z) coordinate systems.

Keywords: multi-phase flow, Moment of fluid method, Interface

---

[1] G. Li and Y. Lian acknowledge the support from General Electric. M. Sussman and M. Jemison acknowledge the support by the National Science Foundation under contract DMS 1016381. M. Arienti acknowledges the support by Sandia National Laboratories via the Laboratory Directed Research and Development program. Sandia National Laboratories is a multi-program laboratory managed and operated by Sandia Corporation, a wholly owned subsidiary of Lockheed Martin Corporation, for the U. S. Department of Energy's National Nuclear Security Administration under contract DE-AC04-94AL85000.

Preprint submitted to International Journal for Numerical Methods in Fluids June 22, 2015 reconstruction, Interface advection, contact line dynamics, triple junctions, gas-liquid jet flow, droplet impact, droplet collision

---

1. Introduction

Multiphase flow plays an important role in many technical applications including ink-jet printing, spray cooling, icing, combustion and agricultural irrigation. The instability of the interface, mass and heat transfer across the interface, and phase change make multiphase flow problems challenging. Theoretical studies of multiphase flows are mainly based on linear theories (Rayleigh, 1878; Taylor, 1963) but yet most phenomena in multiphase flows display nonlinear feedback mechanisms. Modern experimental studies employ high-speed cameras, pulsed shadowgraph, and holograph techniques (Sallam et al., 1999, 2004; Palacios et al., 2010) in order to understand the complex processes in multiphase flows, nonetheless, it is still very difficult to capture the detailed flow fields.

Computational fluid dynamics (CFD) has the potential to increase ones' understanding of multiphase flow phenomena by allowing one to investigate flow fields deeply embedded within materials, study the effect of random fluctuations, and allowing one to precisely control initial and boundary conditions. Quantities such as interface surface area, streamlines, stress fields, and vorticity are easily extracted from CFD simulations. Three major challenges exist for the accurate and efficient computation of multiphase flows. First, the density and viscosity ratios between different phases can be high and it is difficult to accurately calculate the flux during the momentum advection (Raessi, 2008; Raessi and Pitsch, 2009). Second, surface tension takes effect only at the interface between different phases and this singularity may cause problems when solving the Navier-Stokes equations (Brackbill et al., 1992; Desjardins et al., 2008). Third, the drastic change of interface topology and disparity in length scales make interface capturing and interface advection challenging (Ménard et al., 2007; Li et al., 2010).

Among the different interface capturing methods, the volume-of-fluid (VOF) method (Hirt and Nichols, 1981; Brackbill et al., 1992; Pilliod Jr and Puckett, 2004) , the level set method (Osher and Sethian, 1988; Sussman et al., 1994, 1998, 1999; Osher and Fedkiw, 2001) and their derivatives are widely used.

The VOF method tracks the volume fraction function within each computational grid cell. The interface is reconstructed and advected based on the volume fraction function information. The benefit of VOF methods is that there have been devised either directionally split advection algorithms Rudman (1998); Scardovelli and Zaleski (2003); Jemison et al. (2013); Weymouth and Yue (2010) or unsplit advection algorithms (Liovic et al., 2006; Chenadec and Pitsch, 2013; Jemison et al., 2015) which have excellent volume preservation properties.

The level set method uses a smooth distance function to implicitly represent the interface. On the one hand, the level set method is amenable to computing flows with surface tension effects since the distance function is smooth across the interface, on the other hand, volume conservation for the level set method is not guaranteed, even if the level set advection equation is discretized in conservation form. The coupled level set and volume-of-fluid (CLSVOF) method (Sussman and Puckett, 2000; Son and Hur, 2002; Sussman, 2003; Ménard et al., 2007; Wang et al., 2009) has also been developed. Even though the specific implementations of CLSVOF methods vary, the overriding theme of CLSVOF methods is that they maintain the advantages of both the level set method and the VOF method in simultaneously conserving volume and accurately capturing the interface (Sussman and Puckett, 2000; Wang et al., 2009).

Recently, the moment of fluid (MOF) method (Dyadechko and Shashkov, 2005; Ahn and Shashkov, 2007; Dyadechko and Shashkov, 2008; Ahn and Shashkov, 2009; Ahn et al., 2009; Jemison et al., 2013, 2014, 2015) has been developed. In addition to the volume fraction function used in the VOF method, the MOF method considers the material centroid information in the interface reconstruction process and can be considered a generalization of the VOF method. The MOF interface reconstruction is completely local because of the introduction of centroid information. This feature enables the MOF method to capture corners and sheets significantly better than the VOF method for passively advected flows. Results of benchmark tests comparing MOF to VOF and CLSVOF are reported in (Kucharik et al., 2010; Wang et al., 2012; Jemison et al., 2013). A further advantage of the moment of fluid representation is that the added centroid information enables the MOF method to straightforwardly reconstruct any number of materials, i.e. two or more, in a given cell, conserving volume of each material (Ahn and Shashkov, 2007; Jemison et al., 2015).

We remark that there have previously been developed the following VOF triple junction reconstruction algorithms: the "onion skin" approach in which the materials do not intersect (Sijoy and Chaturvedi, 2010), the material order independent weighted Voronoi diagram (also known as a power diagram) approach for 2D reconstruction of triple points applied to static configurations (Schofield et al., 2008), an optimization method for the localization of the triple point applied to 2D passive transport problems (Caboussat et al., 2008), and an improved material order independent weighted Voronoi diagram approach in which a novel optimization procedure was developed for determining interface(s) normals (Schofield et al., 2009).

We have taken the "nested dissection" MOF approach; if a computational cell contains M materials, then there will be $M-1$ linear cuts in the cell, some cuts potentially intersecting previous cuts. The MOF algorithm can reconstruct interface configurations where 3 materials meet at a single point, albeit one of the angles separating 2 of the materials must be 90 degrees.

In this paper, we describe a novel method in which we use the MOF multimaterial reconstruction algorithm in order to simulate incompressible multiphase flow in two or three dimensions in which (i) two fluids with disparate material properties can meet at a third rigid material (contact line dynamics) and (ii) three fluids with disparate material properties meet at a triple junction. As in (Jemison et al., 2014), we maintain and update the velocity at both cell centers and face centers. The velocity is interpolated from cell centers to face centers using mass weighting where the MOF reconstruction determines the weights. Pressure is interpolated from cell centers to face centers using the condition of constant contact, where again the weights depend on the MOF reconstructed interface.

In what follows we describe our incompressible multi-phase MOF method, and we describe the algorithm that we have developed for the simulation of contact line dynamics and triple point dynamics. Example simulations are given with validations through grid refinement studies and comparisons with experiments and finally conclusions are drawn.

2. Governing equations

The governing equations for incompressible, immiscible, multiphase flows are:

$$\nabla \cdot \boldsymbol{u} = 0 \tag{1}$$

$$\frac{\partial \phi_m}{\partial t} + \boldsymbol{u} \cdot \nabla \phi_m = 0, \quad m = 1, \ldots, M \tag{2}$$

$$\frac{\partial \boldsymbol{u}}{\partial t} + \boldsymbol{u} \cdot \nabla \boldsymbol{u} = -\frac{\nabla p_m}{\rho_m} + \frac{\nabla \cdot (2\mu_m D)}{\rho_m} + \boldsymbol{g} \quad \text{if } \phi_m(\boldsymbol{x}, t) > 0 \tag{3}$$

where ϕ_m is a level set function for material m and satisfies,

$$\phi_m(\boldsymbol{x}, t) = \begin{cases} > 0 & \boldsymbol{x} \in \text{ material } m \\ \leq 0 & \text{otherwise} \end{cases}$$

$\boldsymbol{u} = (u, v, w)$ is the velocity vector, t is the time, p_m is the pressure for material m, $\boldsymbol{g}$ is the gravitational acceleration vector, D is the rate of deformation tensor,

$$D = \frac{\nabla \boldsymbol{u} + (\nabla \boldsymbol{u})^T}{2},$$

and μ_m and ρ_m are the viscosity and density respectively for material m.

At material interfaces, if there is no mass transfer, the velocity for all materials are the same. For two phase flow problems ($M = 2$), at a material interface that separates material m_1 from m_2 (i.e. $\phi_{m_1}(\boldsymbol{x}, t) = \phi_{m_2}(\boldsymbol{x}, t) = 0$), the stress will have the following jump condition due to the effect of the surface tension force,

$$((-p_{m_1} I + 2\mu_{m_1} D) - (-p_{m_2} I + 2\mu_{m_2} D)) \cdot \boldsymbol{n}_{m_1} = \sigma_{m_1,m_2} \kappa_{m_1} \boldsymbol{n}_{m_1}$$

where σ_{m_1,m_2} is the surface tension coefficient, the normal that points from material m_2 into m_1 is,

$$\boldsymbol{n}_{m_1} = \frac{\nabla \phi_{m_1}}{|\nabla \phi_{m_1}|},$$

and the curvature is,

$$\kappa_{m_1} = \nabla \cdot \frac{\nabla \phi_{m_1}}{|\nabla \phi_{m_1}|}.$$

An one-fluid formulation of (3) can be written as follows (Kim, 2007):

$$\frac{\partial \rho \boldsymbol{u}}{\partial t} + \nabla \cdot (\rho \boldsymbol{u} \otimes \boldsymbol{u}) = -\nabla p + \nabla \cdot (2\mu D) + \rho \boldsymbol{g} - \sum_{m=1}^{M} \gamma_m \kappa_m \nabla H(\phi_m) \tag{4}$$

where $H(\phi)$ is the Heaviside function defined as,

$$H(\phi) = \begin{cases} 1 & \phi \geq 0 \\ 0 & \text{otherwise} \end{cases}, \tag{5}$$

the combined density ρ is,

$$\rho = \sum_{m=1}^{M} \rho_m H(\phi_m),$$

the combined viscosity, μ, is,

$$\mu = \sum_{m=1}^{M} \mu_m H(\phi_m),$$

and (3 material case):

$$\gamma_1 = \frac{\sigma_{12} + \sigma_{13} - \sigma_{23}}{2} \tag{6}$$

$$\gamma_2 = \frac{\sigma_{12} + \sigma_{23} - \sigma_{13}}{2} \tag{7}$$

$$\gamma_3 = \frac{\sigma_{13} + \sigma_{23} - \sigma_{12}}{2} \tag{8}$$

3. Numerical method

We describe our numerical method for two dimensional problems, but the method is straightforwardly generalizable to three dimensions.

3.1. Overview of the method

The numerical method, which is based on an approximate projection method (Jemison et al., 2013), is given in the following list of steps. The spatial discretization details for each step are explained in the ensuing sections.

1. At the beginning of the time step $t = t^n$, and in each computational cell,

$$\Omega_{i,j} = \{\boldsymbol{x} : x_i - \Delta x/2 < x < x_i + \Delta x/2, y_j - \Delta y/2 < y < y_j + \Delta y/2\},$$

the following variables are given: mass weighted average of velocity $(\boldsymbol{u}^n_{i,j})$, Discretely, divergence free velocity on MAC grid,

$$\frac{u^{MAC,n}_{i+1/2,j} - u^{MAC,n}_{i-1/2,j}}{\Delta x} + \frac{v^{MAC,n}_{i,j+1/2} - v^{MAC,n}_{i,j-1/2}}{\Delta y} = 0,$$

volume fraction, $F^n_{m,i,j}$, and centroid, $\boldsymbol{x}^n_{m,i,j}$, for each material m. Figure 1 illustrates our discretization.

2.Advection: Referring to (4) and (2), the directionally split cell integrated semi-Lagrangian (CISL) method is used to solve the following equations:

$$(\rho \boldsymbol{u})_t + \nabla \cdot (\rho \boldsymbol{u} \otimes \boldsymbol{u}) = 0 \tag{9}$$

$$(F_m)_t + \nabla \cdot (\boldsymbol{u} F_m) = 0 \tag{10}$$

The details of CISL advection are given in section 3.2.

3. Distance functions: Distance functions, $\phi_{m,i,j}^{n+1}$, are derived from the non-tessellating MOF reconstructed interface for each material $m = 1, \ldots, M$. The distance functions are used to approximate interface curvature. See section 3.3.

4. Viscosity, gravity, surface tension: Referring to (4),

$$\boldsymbol{V} = \boldsymbol{u}^{advect} + \Delta t \frac{1}{\rho} \left(\nabla \cdot (2\mu D) + \rho \boldsymbol{g} - \sum_{m=1}^{M} \gamma_m \kappa_m \nabla H(\phi_m) \right) \tag{11}$$

See sections 3.4 and 3.5.

5. Approximate projection: A variable density approximate projection algorithm is used to discretize the pressure gradient force,

$$\boldsymbol{u}^{n+1} = \boldsymbol{V} - \Delta t \frac{\nabla p}{\rho},$$

where p solves,

$$\nabla \cdot \frac{\nabla p}{\rho} = \frac{1}{\Delta t} \nabla \cdot \boldsymbol{V}.$$

See section 3.6

6. The block structured adaptive grid is regenerated depending on the new locations of material interfaces and then the algorithm returns back to step 2.

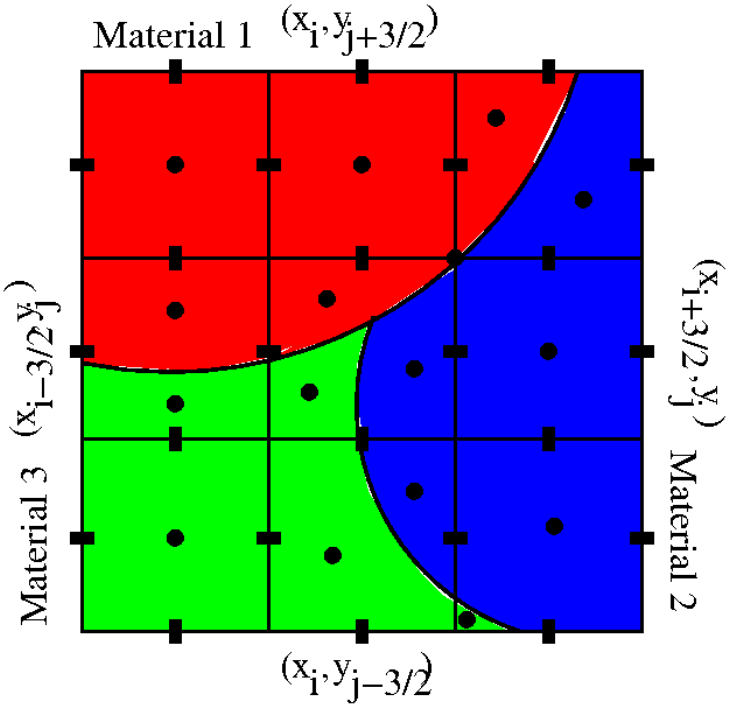

Figure 1: The volume fractions F_m, centroids $\boldsymbol{x}_m$ (filled in circles), and cell centered velocity, $\boldsymbol{u}$, are cell averaged quantities, and the face centered velocity (filled in rectangles), u^{MAC}, v^{MAC} are face averaged quantities. There are 3 materials illustrated in this figure. The center coordinate of the illustrated 3x3 block of cells is (x_i, y_j).

3.2. Directionally Split CISL Multiphase Advection

The CISL algorithm has three parts: (i) interface reconstruction, (ii) momentum reconstruction, and (ii) mapping of reconstructed solution into computational cells from a given cells' preimage.

3.2.1. Moment of Fluid Interface Reconstruction

The moment-of-fluid method(Dyadechko and Shashkov, 2005; Ahn and Shashkov, 2007; Dyadechko and Shashkov, 2008; Ahn and Shashkov, 2009; Jemison et al., 2013) is used to represent material interfaces. For a computational cell $\Omega_{i,j}$, the volume fraction (zeroth order moment) and centroid (first order moment) are:

$$F_m = \frac{1}{|\Omega_{i,j}|} \int_{\Omega_{i,j}} H(\phi_m(\boldsymbol{x})) d\boldsymbol{x},$$

$$\boldsymbol{x}_m = \frac{\int_{\Omega_{i,j}} H(\phi_m(\boldsymbol{x}))\boldsymbol{x} d\boldsymbol{x}}{\int_{\Omega_{i,j}} H(\phi_m(\boldsymbol{x})) d\boldsymbol{x}}.$$

When there are two materials in a cell, the material interface is reconstructed as a plane in three-dimensions (3D) and a line in two-dimensions (2D). This interface representation is called the piecewise linear interface calculation (PLIC). Take a 2D case for example, an interface Γ in cell $\Omega_{i,j}$ is represented by a straight line as shown in Fig. 2 using the following vector form equation:

$$\Gamma = \Omega_{i,j} \cap \{\boldsymbol{x} | \boldsymbol{n} \cdot (\boldsymbol{x} - \boldsymbol{x}_{i,j}) + b = 0\} \tag{12}$$

where $\boldsymbol{n}$ is the interface unit normal vector, $\boldsymbol{x}_{i,j}$ is the cell center of $\Omega_{i,j}$ and b is the distance from $\boldsymbol{x}_{i,j}$ to the interface. Thus, the interface can be constructed when the normal vector $\boldsymbol{n}$ and distance b are known.

In order to find the slope and intercept of the reconstructed plane (line in 2D), we use the reference volume fraction, F_{ref}, and the reference centroid, $\boldsymbol{x}^c_{ref}$. The reference volume fraction and centroid correspond to the real interface which is not necessarily a straight line. The slope $\boldsymbol{n}$ and intercept b are selected so that the actual volume fraction function $F_{act} = F_{act}(\boldsymbol{n}, b)$ is equal to F_{ref} and the actual centroid, $\boldsymbol{x}^c_{act}(\boldsymbol{n}, b)$ is as close as possible to $\boldsymbol{x}^c_{ref}$. In other words, $\boldsymbol{n}$ and b are chosen in order to minimize E_{MOF} (13) subject to the volume fraction constraint given in (14):

$$E_{MOF} = \|\boldsymbol{x}^c_{ref} - \boldsymbol{x}^c_{act}(\boldsymbol{n}, b)\|_2 \tag{13}$$

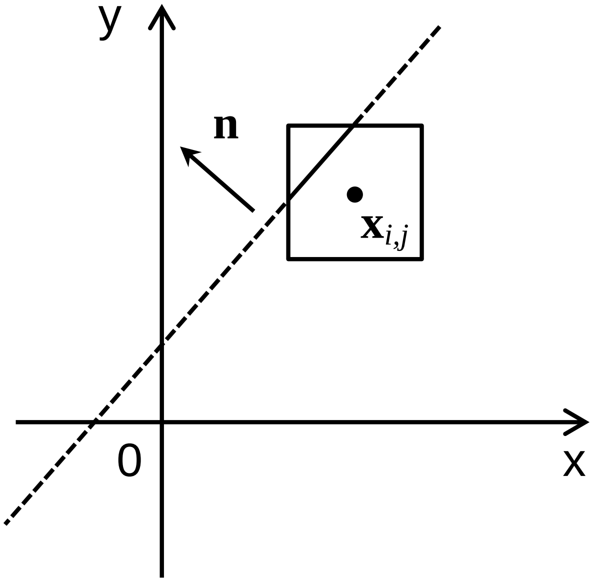

Figure 2: The gas-liquid interface is represented by a straight line in 2D. The square represents a computational cell and $\boldsymbol{x}_{i,j}$ is the coordinate of the cell center.

$$|F_{ref} - F_{act}(\boldsymbol{n}, b)| = 0 \tag{14}$$

An example of a real interface and the corresponding reconstructed interface is illustrated in Fig. 3. The curved solid line in the left figure represents the true interface and the dashed line in the right figure is the reconstructed interface. In Fig. 3 $\boldsymbol{x}^c_{ref}$ is the centroid of the reference interface whose volume fraction F_{ref} is the blue area under the solid curved line, and $\boldsymbol{x}^c_{act}$ is the computed centroid of the actual reconstructed interface whose volume fraction F_{act} is the blue area under the dashed straight line.

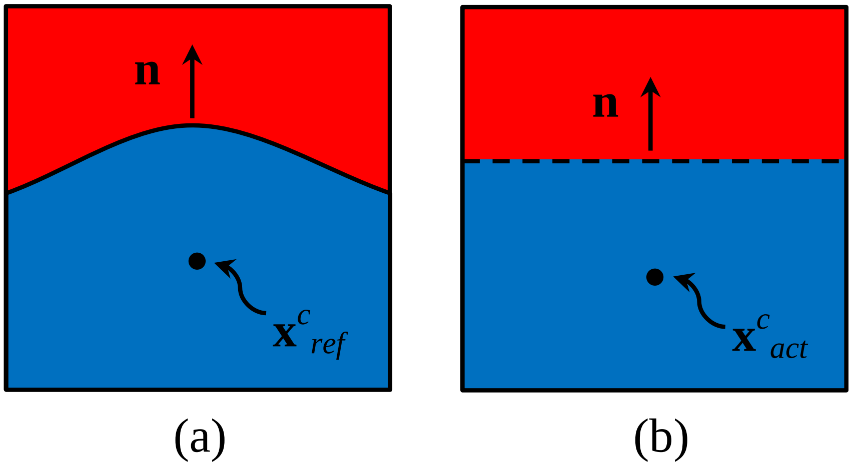

Figure 3: MOF interface reconstruction. The solid curved line on the left represents the real interface and the dashed straight line on the right is the reconstructed interface.

Since the normal vector $\boldsymbol{n}$ can be parametrized using the following equation

$$\boldsymbol{n} = \begin{pmatrix} sin(\Phi)cos(\Theta) \\ sin(\Phi)sin(\Theta) \\ cos(\Phi) \end{pmatrix} \tag{15}$$

E_{MOF} becomes a function of angles Φ and Θ. Therefore, we need to find (Φ^*, Θ^*) such that

$$E_{MOF}(\Phi^*, \Theta^*) = \|f(\Phi^*, \Theta^*)\|_2 = min\|f(\Phi, \Theta)\|_2 \tag{16}$$

where

$$f(\Phi, \Theta) = \boldsymbol{x}_{ref}^c - \boldsymbol{x}_{act}^c(\Phi, \Theta)$$

The problem becomes a non-linear least square problem for (Φ, Θ). Eq. 16 is solved numerically by the Gauss-Newton algorithm and the detailed step-by-step procedure is as follows:

0. choose initial angles (Φ_0, Θ_0) and set tolerance $tol = 10^{-8}\Delta x$ with Δx the grid size.

while not converged set $k = 1$

1. find $b_k(\Phi_k, \Theta_k)$ such that Eq. 14 holds
2. find centroid $\boldsymbol{x}_k^c(b_k, \Phi_k, \Theta_k)$
3. find Jacobian matrix J_k of f evaluated at (Φ_k, Θ_k) and $f_k = f(\Phi_k, \Theta_k)$
4. stop if one of the three conditions is fulfilled:
   - $\|J_k^T \cdot f_k\| < tol \cdot 10^{-2}\Delta x$
   - $\|f_k\| < tol$
   - $k = 11$
5. solve the linear least squares problem,

   $$s_k = \text{argmin}_s |J_k s + f_k|_2,$$

   using the normal equations: $J_k^T J_k s_k = J_k^T f_k$.
6. update the angles: $(\Phi_{k+1}, \Theta_{k+1}) = (\Phi_k, \Theta_k) + s_k$
7. $k := k + 1$ and go back to step 1.

The detailed process for the minimization of Eq. 13 can be found in (Jemison et al., 2013). Unlike the VOF method, the MOF interface reconstruction method only uses information from the computational cell under consideration. This property makes the MOF method more suitable for deforming boundary problems with sharp corners, with slender filaments, or containing greater than two materials. Also, the MOF reconstruction algorithm makes itself more suitable for block structured dynamic adaptive mesh refinement since conditions at coarse/fine grid interface can be interpolated from the coarse grid using a stencil that does not depend circularly on the neighboring fine grid.

When there are greater than two materials in cell $(M > 2)$ $\Omega_{i,j}$, the following extension of the two-material MOF reconstruction procedure determines M polygonal regions, Ω_m, that tessellate $\Omega_{i,j}$ (see Figure 4):

1. Initialize $p = 0$ where p is a counter that represents, at any given iteration, the number of materials (polygons) that have already been reconstructed in cell $\Omega_{i,j}$. The uncaptured space in this cell is initialized as,

$$\Omega_u^p = \Omega_{i,j}, \tag{17}$$

where $\Omega_{i,j}$ represents cell (i, j). The centroid of Ω_u^p is denoted as $\boldsymbol{x}_u^p$. Tag all materials as "not defined."

2. In the cell identify the material whose centroid ($\boldsymbol{x}_{i,j}^m$) is furthest to the uncaptured centroid $\boldsymbol{x}_u^p$ among all "not defined" materials, i.e.,

$$m^p = \text{argmax}_{m,F_{i,j}^m>0,m\text{not defined}}|\boldsymbol{x}_{i,j}^m - \boldsymbol{x}_u^p|. \tag{18}$$

3. Calculate the slope $\hat{\boldsymbol{n}}$ and intercept b that minimizes the centroid error with the constraint that $|F_{act}^{m^p}(\hat{n}, b) - F_{ref}^{m^p}| = 0$ and construct the MOF interface. Ω_{m^p} is defined as:

$$\Omega_{m^p} = \Omega_u^p \cap \{\boldsymbol{x}|\hat{n} \cdot (\boldsymbol{x} - \boldsymbol{x}_{i,j}) + b \geq 0\} \tag{19}$$

The Gauss-Newton method as written for the 2-material scenario is used to solve the optimization problem. Tag material m as "defined."

4. Update Ω_u^{p+1}

$$\Omega_u^{p+1} = \Omega_u^p \cap \Omega_{m^p}^{Complement} \tag{20}$$

5. Let $p = p + 1$ and go back to step 2.

As a remark on determining volumes and moments of polygonal regions, in contrast to earlier implementations of the Moment-of-Fluid Interface Reconstruction method that used a Gauss-Green discretization to compute volumes and moments of polygonal regions (Ahn and Shashkov, 2007), our implementation makes use of triangulation (tetrahedralization in 3D) to compute reference volumes and reference centroids. Rectangular cells are subdivided into triangles. The intersection of two triangular (tetrahedral) regions is expressed as the union of multiple triangular (tetrahedral) regions. A lookup table is utilized to efficiently cut a triangle (tetrahedron) with a

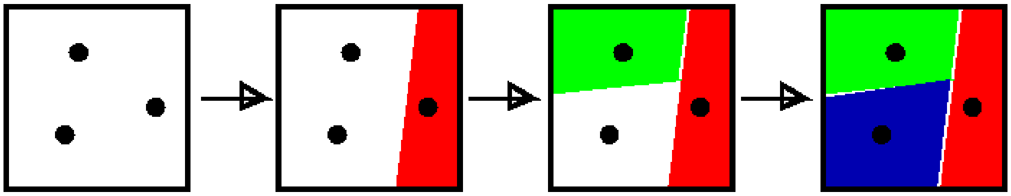

Figure 4: Illustration of volume preserving and tessellating MOF reconstruction with three materials; in order to conserve volume, the MOF reconstruction must tessellate a cell when it is used for advection (section 3.2.3). The uncaptured region is initialized as the whole cell, $\Omega_u^0 = \Omega_{i,j}$, and then progressively reduced as each new material m fills the cell: $\Omega_u^{p+1} = \Omega_u^p \cap \Omega_{m^p}^{Complement}$. The solid circles are the reference first order moments for each material.

linear (planar) interface and triangulate (tetrahedralize) the cut region. Volume of the cut region is then computed as the sum of the volumes of the constituent triangles (tetrahedra). Since all polygonal (polyhedral) regions are decomposed into triangles (tetrahedra), it is easy to compute moments. For a given triangle (tetrahedra) T, the centroid $\boldsymbol{x}_T$ is the average of its vertices $\boldsymbol{x}_j$ shown as follows:

$$\boldsymbol{x}_T = \frac{\int_T \boldsymbol{x} \cdot d\boldsymbol{x}}{\int_T d\boldsymbol{x}} = \frac{1}{3}\sum_{j=1}^{3} \boldsymbol{x}_j \tag{21}$$

Any polygonal region P that we consider can be written as the union of N triangles T_i,

$$P = \bigcup_{i=1}^{N} T_i. \tag{22}$$

If each triangle has volume V_i and centroid $\boldsymbol{x}_{T_i}$, then the volume V_P of the region P is equal to the sum of the volumes of T_i and the centroid $\boldsymbol{x}_P$ of P is the volume-weighted sum of the centroids:

$$V_P = \sum_{i=1}^{N} V_i \tag{23}$$

$$\boldsymbol{x}_P = \frac{\int_P \boldsymbol{x} \cdot d\boldsymbol{x}}{\int_P d\boldsymbol{x}} = \frac{\sum_{i=1}^{N} V_i \boldsymbol{x}_{T_i}}{V_P} \tag{24}$$

3.2.2. MINMOD piecewise linear reconstruction of the momentum for each material

Without loss of generality, we describe the piecewise linear, MINMOD slope limited, momentum reconstruction procedure for directionally split CISL advection in the x direction in cell $\Omega_{i,j}$:

1. Initialize momentum for material m from density and velocity:

$$\boldsymbol{U}^n_{m,i',j} \equiv \rho_m \boldsymbol{u}^n_{i',j} \quad i' = i-1, i, i+1$$

2. Initialize the slope for the linear reconstruction:

$$\boldsymbol{U}'_{i,j} = \begin{cases} 0 & (D_+\boldsymbol{U}_{i,j})(D_-\boldsymbol{U}_{i,j}) \le 0 \\ \mathbf{SGN} \cdot \min(|\frac{D_+\boldsymbol{U}_{i,j}}{\Delta x}|, |\frac{D_-\boldsymbol{U}_{i,j}}{\Delta x}|) & \text{otherwise} \end{cases}$$

$$D_+\boldsymbol{U}_{i,j} \equiv \boldsymbol{U}_{i+1,j} - \boldsymbol{U}_{i,j} \quad D_-\boldsymbol{U}_{i,j} \equiv \boldsymbol{U}_{i,j} - \boldsymbol{U}_{i-1,j} \quad \mathbf{SGN} \equiv \frac{D_+\boldsymbol{U}_{i,j}}{|D_+\boldsymbol{U}_{i,j}|}$$

3. The slope limited reconstruction of the momentum for material m is now:

$$\boldsymbol{\mathcal{U}}^n_{m,i,j}(x) = (\boldsymbol{U}')^n_{m,i,j}(x - x^n_{m,i,j}) + \boldsymbol{U}^n_{m,i,j} \tag{25}$$

3.2.3. Directionally split mapping of reconstructed solution into a target cell $\Omega_{i,j}$

We have implemented two different directional splitting advection algorithms. The first directionally split algorithm that we implemented is based on the alternating Eulerian-Implicit Lagrangian Explicit (EI-LE) algorithm described in (Scardovelli and Zaleski, 2003) and (Aulisa et al., 2007). In two-dimensions, we advect in the X direction first using Eulerian-Implicit (EI) time discretization (backwards tracing) and then we advect in the Y direction using the Lagrangian-Explicit (LE - forwards tracing) time discretization. In 3D, the advection ordering is X (EI), Y (LE), and Z (EI). The ordering is reversed every time step so that in 2D, for this example, the next time step would involve (EI) advection in the Y direction, followed by (LE) advection in the X direction. The alternating approach exactly conserves volume for each material in two dimensions, but not in three dimensions and not using an axisymmetric R-Z coordinate system.

The second directionally split algorithm that we implemented follows the algorithm described in (Weymouth and Yue, 2010). The approach advects in the X and Y (X-Y-Z in 3D) directions using the Eulerian Implicit (EI - backwards tracing) scheme and then reverses the direction ordering at the next time step. In a given cell $\Omega_{i,j}$, the Weymouth and Yue algorithm for advection in 2D solves the following equations in which the initial condition at time $t = t^n$, F^n, is given:

$$\begin{array}{rcl} \begin{array}{r} F_\tau + (uF)_x = 0 \\ F_\tau + (vF)_y = 0 \end{array} & \begin{array}{c} 0 \le \tau \le \Delta t \\ \Delta t \le \tau \le 2\Delta t \end{array} & \text{if } F^n_{i,j} < 1/2 \\ \begin{array}{r} F_\tau + (uF)_x = u_x \\ F_\tau + (vF)_y = v_y \end{array} & \begin{array}{c} 0 \le \tau \le \Delta t \\ \Delta t \le \tau \le 2\Delta t \end{array} & \text{if } F^n_{i,j} \ge 1/2 \end{array}$$

Remarks:

- If the face velocity is discretely divergence free, then the EI-LE method is free stream preserving and conserves volume exactly in 2D.
- If the face velocity is discretely divergence free, then the Weymouth and Yue algorithm preserves volume exactly in 2D, 3D axisymmetric, and 3D coordinate systems. Albeit, the Weymouth and Yue algorithm has a more stringent time step constraint in 3D,

  $$|U|\Delta t < \frac{\Delta x}{6},$$

  than for the EI-LE approach,

  $$|U|\Delta t < \frac{\Delta x}{2}.$$

Here we illustrate the details for the backwards projection and forwards projection, but only in the x direction. The CISL algorithm in the y and z directions is carried out analogously.

For backwards tracing of characteristics, the CISL mapping function is,

$$T^{CISL}_{i,j}(x, y) = (\alpha x + \beta, y)$$

in which α and β are chosen so that,

$$T^{CISL}_{i,j} : \Omega^{depart}_{i,j} \to \Omega^{target}_{i,j},$$

where,

$$\begin{aligned}
x_{Left} &= x_{i-1/2} - \Delta t u_{i-1/2} \\
x_{Right} &= x_{i+1/2} - \Delta t u_{i+1/2} \\
\Omega_{i,j}^{depart} &= \{(x,y)|x_{Left} < x < x_{Right}, y_{j-1/2} < y < y_{j+1/2}\} \\
\Omega_{i,j}^{target} &= \{(x,y)|x_{i-1/2} < x < x_{i+1/2}, y_{j-1/2} < y < y_{j+1/2}\} \\
\alpha &= \frac{\Delta x}{x_{Right} - x_{Left}} \\
\beta &= x_{i-1/2} - \alpha x_{Left}.
\end{aligned}$$

For forwards tracing of characteristics, the mapping function is a piecewise linear function broken up into three parts, $i' = -1, 0, 1$:

$$T_{i,j}^{CISL}(x,y) = \begin{cases} \tilde{T}_{i-1,j}^{CISL}(x,y) & \text{if } \tilde{T}_{i-1,j}^{CISL}(x,y) \in \Omega_{i,j} \\ \tilde{T}_{i,j}^{CISL}(x,y) & \text{if } \tilde{T}_{i,j}^{CISL}(x,y) \in \Omega_{i,j} \\ \tilde{T}_{i+1,j}^{CISL}(x,y) & \text{if } \tilde{T}_{i+1,j}^{CISL}(x,y) \in \Omega_{i,j} \end{cases}$$

$$\begin{aligned}
\tilde{T}_{i+i',j}^{CISL}(x,y) &= (\alpha x + \beta, y) \\
x_{Left} &= x_{i+i'-1/2} + \Delta t u_{i+i'-1/2} \\
x_{Right} &= x_{i+i'+1/2} + \Delta t u_{i+i'+1/2} \\
\alpha &= \frac{x_{Right} - x_{Left}}{\Delta x} \\
\beta &= x_{Left} - \alpha x_{i+i'-1/2}.
\end{aligned}$$

In Figures (5) and (6) we illustrate the backwards and forwards tracing of characteristics respectively. In Figure (5), the departure region,

$$\Omega_{i,j}^{depart} \equiv (T_{i,j}^{CISL})^{-1}(\Omega_{i,j}),$$

is intersected with each reconstructed (polygonal) material region in neighboring cells; this is denoted by $V_{-1,i}^{n}$ and $V_{0,i}^{n}$ in Figure (5). Then these material regions, and the momentum within these regions, are mapped forward under the action of $T_{i,j}^{CISL}$ in order to form the material regions at the new time:

$$\begin{aligned}
V_{-1,i}^{n+1} &= T_{i,j}^{CISL}(V_{-1,i}^{n}) \\
V_{0,i}^{n+1} &= T_{i,j}^{CISL}(V_{0,i}^{n})
\end{aligned}$$

So, for either the forwards or backwards tracing algorithm, we solve the volume fraction equation (10), centroid equation, and momentum advection equation (9), as follows:

$$F_{m,i,j}^{n+1} = \frac{\sum_{i'=-1}^{1} |T_{i,j}^{CISL}(\Omega_{m,i+i'}^{n}) \cap \Omega_{i,j}|}{|\Omega_{i,j}|} \tag{26}$$

$$\boldsymbol{x}_{m,i,j}^{n+1} = \frac{\sum_{i'=-1}^{1} \int_{T_{i,j}^{CISL}(\Omega_{m,i+i'}^{n}) \cap \Omega_{i,j}} \boldsymbol{x} d\boldsymbol{x}}{F_{m,i,j}^{n+1} |\Omega_{i,j}|} \tag{27}$$

$$\boldsymbol{u}_{m,i,j}^{advect} = \frac{\sum_{i'=-1}^{1} \int_{\Omega_{m,i+i'}^{n} \cap (T_{i,j}^{CISL})^{-1}(\Omega_{i,j})} \boldsymbol{\mathcal{U}}_{m,i+i',j}^{n}(x) d\boldsymbol{x}}{\sum_{i'=-1}^{1} \rho_m |\Omega_{m,i+i'}^{n} \cap (T_{i,j}^{CISL})^{-1}(\Omega_{i,j})|} \tag{28}$$

3.3. Distance functions

In order to approximate the curvature of interfaces (see section 3.5), signed distance functions $\phi_{m,i,j}$ are constructed. $\phi_{m,i,j}$ is the signed distance from the center of cell $\Omega_{i,j}$, $\boldsymbol{x}_{i,j}$, to the piecewise linear (planar in 3D) "tessellating" (in the vicinity of contact lines) or "non-tessellating" (in the vicinity of triple junctions) moment of fluid reconstructed material m interface (See Figure 7). The sign is positive if $\boldsymbol{x}_{i,j} \in \Omega_{m,i,j}$ and negative otherwise.

At a triple point in cell $\Omega_{i,j}$, the "non-tessellating" moment of fluid reconstructed interface is formed as follows (see Figure 7):

> For each material m ($m = 1, \ldots, M$) if $F_m > 0$ then we find the slope $\hat{\boldsymbol{n}}$ and intercept b that minimizes the centroid error with the constraint that $|F_{act}^{m}(\hat{\boldsymbol{n}}, b) - F_{ref}^{m}| = 0$.

The Gauss-Newton method as written in Section 3.2.1 is used to solve the optimization problem. The minimization problem is carried out assuming, for each $m = 1, \ldots, M$, that the uncaptured space Ω_u (17) is the whole cell: $\Omega_u = \Omega_{i,j}$. In comparing Figure 4 to Figure 7, we illustrate the difference between the MOF reconstruction that tessellates a cell and the MOF reconstruction that is not required to tessellate a cell.

Once the piecewise linear (planar in 3D) interfaces are reconstructed, then we find the exact signed distance to these reconstructed interfaces(Sussman and Puckett, 2000).

Remarks:

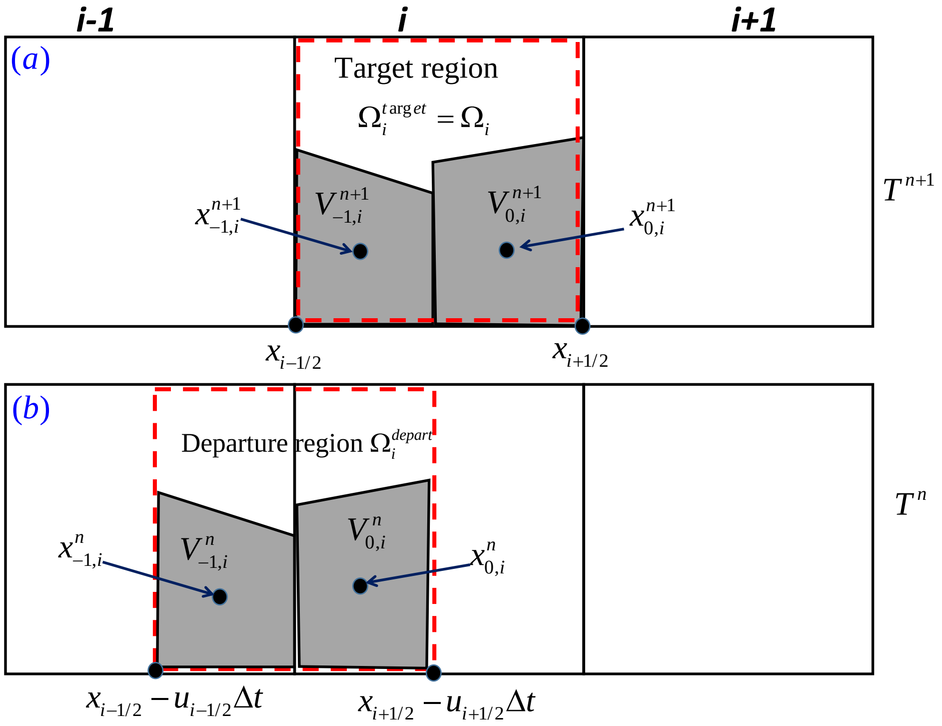

Figure 5: Backward projection for the directionally split method. The dashed rectangle in (b) represents the departure region (Ω_i^{depart}). We denote the departure region of material m as $\Omega_{m,i}^{depart} = V_{-1,i}^n \cup V_{0,i}^n$ which is shaded in (b). $V_{-1,i}^n$ and $V_{0,i}^n$ are the intersection of the departure region with material m in cell $i-1$ and i, respectively, i.e., $V_{-1,i}^n \equiv \Omega_{m,i-1}^n \cap \Omega_i^{depart}$ and $V_{0,i}^n \equiv \Omega_{m,i}^n \cap \Omega_i^{depart}$. $\boldsymbol{x}_{-1,i}^n$ and $\boldsymbol{x}_{0,i}^n$ are the centroid of regions $V_{-1,i}^n$ and $V_{0,i}^n$, respectively. The target region of material m is denoted as $\Omega_{m,i}^{target} = V_{-1,i}^{n+1} \cup V_{0,i}^{n+1}$ which is shaded in (a). The overall target region in (a) is cell i and we denote this as Ω_i^{target}

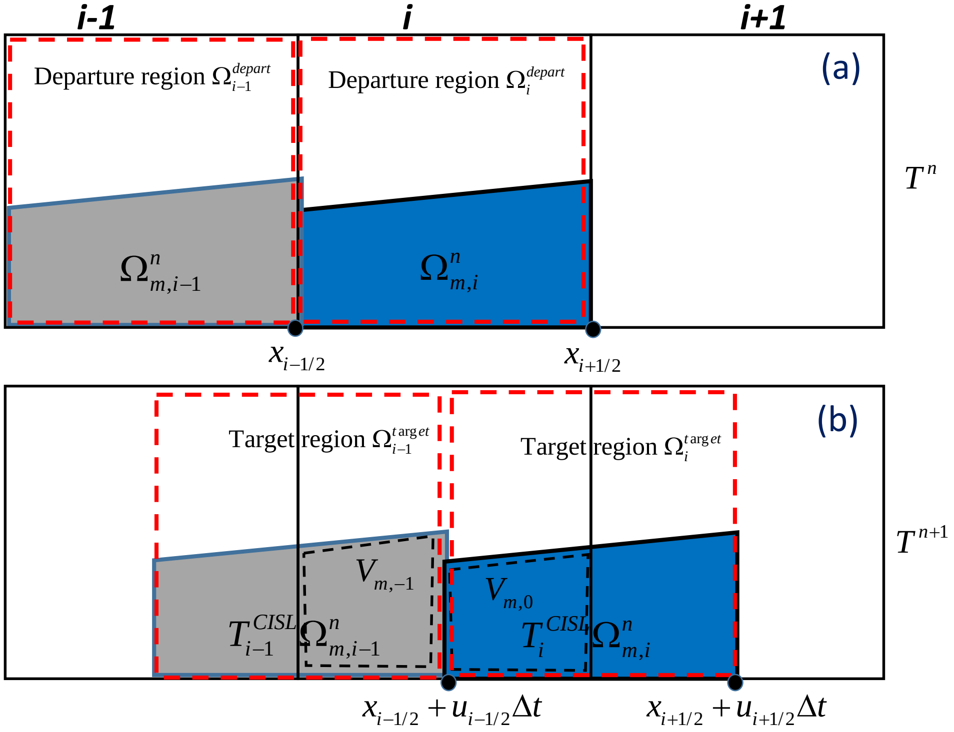

Figure 6: Forward projection for the directionally split method. The dashed rectangles in (b) represent the target regions (Ω_{i-1}^{target} and Ω_{i}^{target}). The departure regions are cells $i-1$ and i in (a). The departure regions of material m in cells $i-1$ and i are $\Omega_{m,i-1}^{n}$ and $\Omega_{m,i}^{n}$, respectively. The target regions of material m are $\tilde{T}_{i-1}^{CISL}\Omega_{m,i-1}^{n}$ and $\tilde{T}_{i}^{CISL}\Omega_{m,i}^{n}$. $V_{m,-1}$ and $V_{m,0}$ are the overlapping regions of the target regions with cell i, i.e., $V_{m,-1} \equiv \tilde{T}_{i-1}^{CISL}(\Omega_{m,i-1}^{n}) \cap \Omega_i$, and $V_{m,0} \equiv \tilde{T}_{i}^{CISL}(\Omega_{m,i}^{n}) \cap \Omega_i$

- As in (Arienti and Sussman, 2014), the signed distance functions ϕ_m representing fluid materials are extrapolated into rigid boundaries. When creating the signed distance to material m, where m represents a fluid, we ignore interfaces that separate m from rigid boundaries. The extrapolated value of $\phi_{m,i,j}$, where $\boldsymbol{x}_{i,j}$ is inside of a rigid body material, is taken as the value of $\phi_{m,i',j'}$ where $\boldsymbol{x}_{i',j'}$ is the closest cell outside of the rigid body to $\boldsymbol{x}_{i,j}$. See Figure 8.

- It is possible for ϕ_m to be positive for more than one value of m and it is also possible that $\phi_m < 0$ for all values of m, so in computational cells $\Omega_{i,j}$ containing a triple junction, we project these distance functions to tessellating distance functions as follows:

$$\phi_m \leftarrow \begin{cases} \phi_m & \text{if } \phi_m \geq 0 \text{ and } m = \text{argmax}_{m'} F_{m'} \\ \phi_m & \text{if } \phi_m < 0 \text{ and } m \neq \text{argmax}_{m'} F_{m'} \\ -\epsilon\Delta x & \text{if } \phi_m \geq 0 \text{ and } m \neq \text{argmax}_{m'} F_{m'} \\ \epsilon\Delta x & \text{if } \phi_m < 0 \text{ and } m = \text{argmax}_{m'} F_{m'} \end{cases} \qquad m = 1, \ldots, M \tag{29}$$

  We assign $\epsilon = 0.01$ in all of our sample calculations.

3.4. Viscosity forces

The viscosity force, $\boldsymbol{F}^{viscous}$, is discretized using a sub-cycling algorithm (Wang et al., 2012):

1. Determine the number of sub-cycling steps, K, such that the following stability condition is satisfied:

$$\frac{\Delta t}{K} \leq \max_{m=1,\ldots,M} \frac{\rho_m}{2\text{DIM}\mu_m} \Delta x^2$$

2. $\boldsymbol{u}^{(0)} = \boldsymbol{u}^{advect}$

3. For $k = 1, \ldots, K$,

$$\boldsymbol{u}^{(k)} = \boldsymbol{u}^{(k-1)} + \frac{\Delta t}{K} \frac{\nabla \cdot (2\mu^{n+1} D^{(k-1)})}{\rho^{n+1}} \tag{30}$$

4. $\boldsymbol{F}^{viscous} = (\boldsymbol{u}^{(K)} - \boldsymbol{u}^{advect})/\Delta t$.

Remarks:

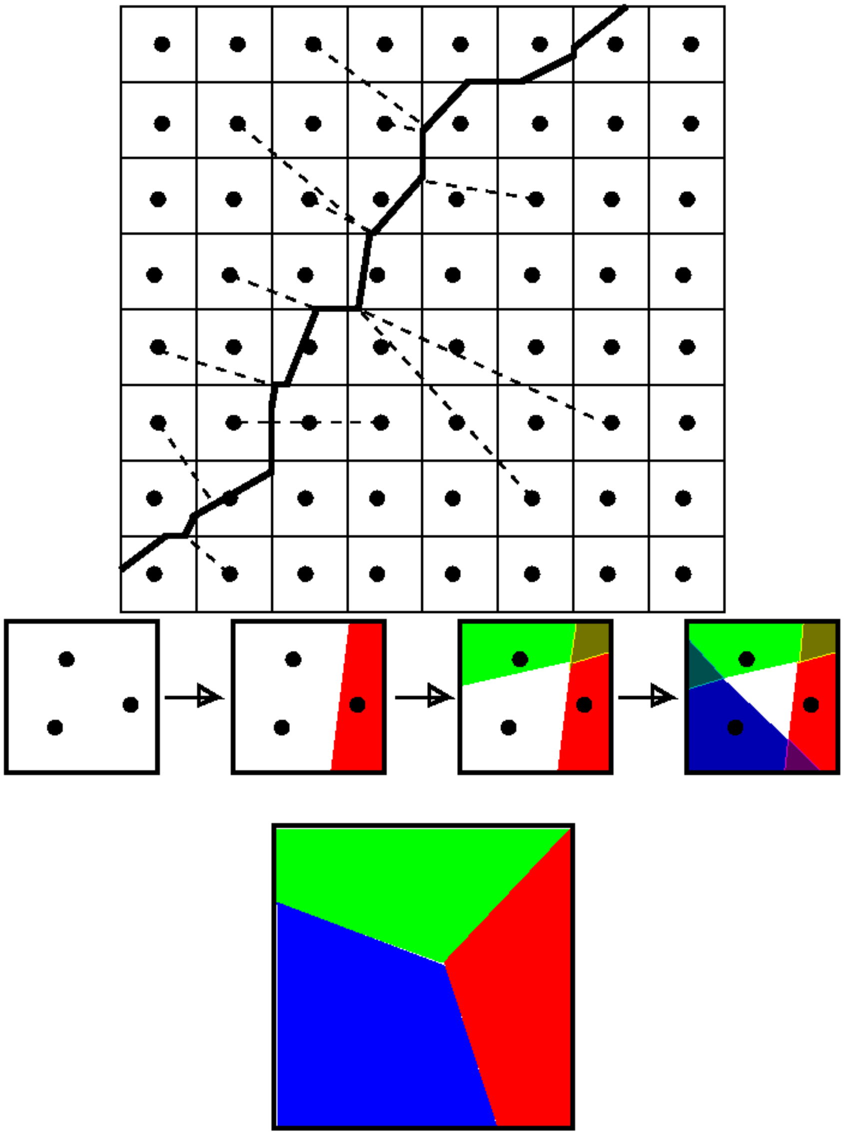

Figure 7: TOP: Signed distance functions ϕ_m are the exact signed distance to the piecewise linear non-tessellating Moment-of-Fluid reconstructed interface. ϕ_m are used to find the curvature (section 3.5). MIDDLE: Illustration of non-tessellating MOF reconstruction. The uncaptured region for each new material is always the whole cell: $\Omega_u = \Omega_{i,j}$. The solid circles are the reference centroids for each material. BOTTOM: The non-tessellating distance functions are projected onto tessellating distance functions in cells containing a triple junction (29).

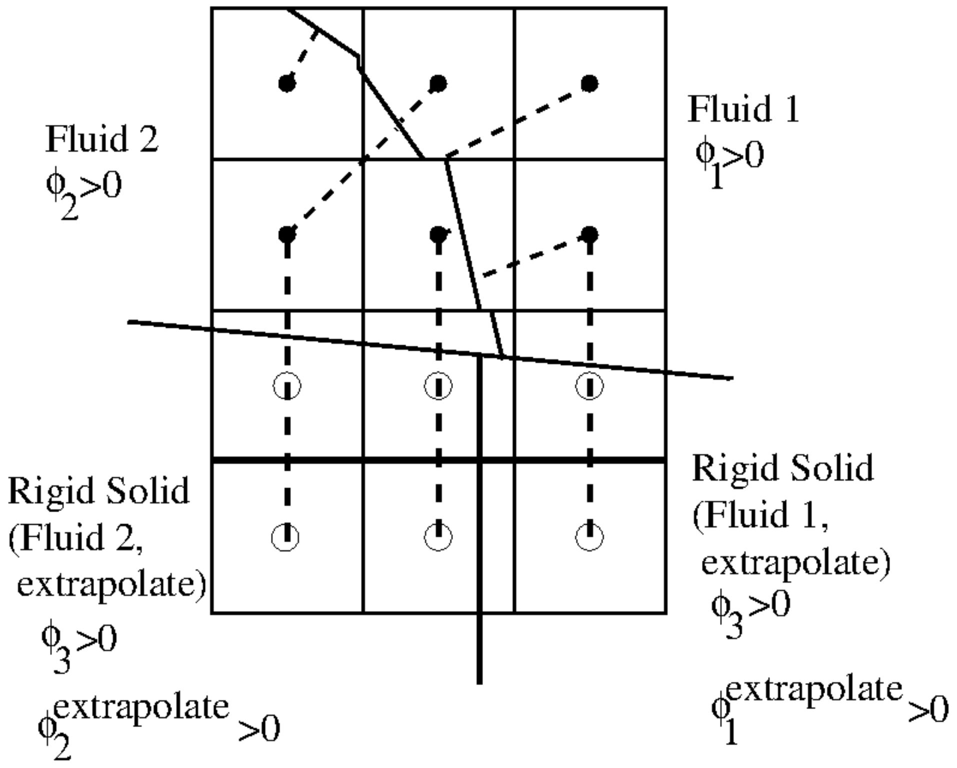

Figure 8: When constructing the distance functions ϕ_1 and ϕ_2 outside of the rigid boundary ($\phi_3 < 0$), the rigid boundary interface is ignored. The thin dashed lines represent the closest distance to the interface separating materials 1 and 2. The values of ϕ_1 and ϕ_2 where $\phi_3 \geq 0$ are extrapolated from the nearest cell in which $\phi_3 < 0$ (thick dashed lines). The extrapolated fluid interface is the thick solid line.

- ρ^{n+1} (30) is written in terms of the volume fractions in multimaterial cells $\Omega_{i,j}$:

$$\rho_{i,j}^{n+1} = \sum_{m=1}^{M} \rho_m F_{m,i,j}^{n+1} \tag{31}$$

- μ^{n+1} (30) is written in terms of the half volume fractions at multimaterial faces $\Omega_{i+1/2,j}$:

$$\mu_{i+1/2} = \frac{\Omega_{i+1/2,j}}{\sum_{m=1}^{M} \frac{1}{\mu_m} \left(|\Omega_{i,j}^m \cap \Omega_{i,R}| + |\Omega_{i+1,j}^m \cap \Omega_{i+1,L}| \right)}.$$

  The regions, $\Omega_{i+1/2,j}$, $\Omega_{i,R}$, and $\Omega_{i+1,L}$ are illustrated in Figure 13 below.

- The spatial discretization of $D^{(k-1)} = (\nabla \boldsymbol{u}^{(k-1)} + (\nabla \boldsymbol{u}^{(k-1)})^T)/2$ is the same as that described in section 3 of (Stewart et al., 2008) in which all terms are discretized using second order central differencing except for the coupling terms in the vicinity of interface(s) separating multiple materials.

3.5. Surface Tension

The spatial discretization of the surface tension force corresponds to the ghost fluid method (Kang et al., 2000) when two materials are present. The surface tension force,

$$-\Delta t \frac{\sigma \kappa \nabla H}{\rho},$$

is discretized at cell faces as,

$$\boldsymbol{F}_{i+1/2,j}^{MAC,tension} \equiv -\Delta t \frac{\sigma \kappa_{i+1/2,j} \left(H(\phi_{i+1,j}) - H(\phi_{i,j}) \right)}{\rho_{i+1/2,j}^{n+1} \Delta x}, \tag{32}$$

where $H(\phi)$ is the Heaviside function (5), ϕ is a signed distance function and $\kappa_{i+1/2,j}$ is the curvature at the point on the interface that crosses inbetween cells $\Omega_{i+1,j}$ and $\Omega_{i,j}$. $\rho_{i+1/2,j}^{n+1} \equiv (\rho_{i,R} + \rho_{i+1,L})/2$ is the density for the face control volume $\Omega_{i+1/2,j}$. $\rho_{i,R}$ and $\rho_{i+1,L}$ are half cell densities (see (46) and (47)).

The surface tension force is discretized at cell centers as,

$$\boldsymbol{F}_{i,j}^{tension} \equiv \frac{\rho_{i,R}\boldsymbol{F}_{i+1/2,j}^{MAC,tension} + \rho_{i,L}\boldsymbol{F}_{i-1/2,j}^{MAC,tension}}{2\rho_{i,j}^{n+1}}. \tag{33}$$

The level set height function method (Arienti and Sussman, 2014; Sussman and Ohta, 2009) is used to approximate the curvature, $\kappa_{i+1/2,j}$, away from triple points and contact lines. Referring to Figure 9, $\kappa_{i+1/2,j}$ in (32) is approximated as follows:

$$\kappa_{i\pm1/2,j} = \left\{ \begin{array}{cc} \kappa_{i,j} & |\phi_{i,j}| < |\phi_{i\pm1,j}| \\ \kappa_{i\pm1,j} & \text{otherwise} \end{array} \right. \tag{34}$$

$$h'' \approx \frac{h_{i+1} - 2h_i + h_{i-1}}{\Delta x^2} \quad h' \approx \frac{h_{i+1} - h_{i-1}}{2\Delta x} \tag{35}$$

$$\kappa_{i,j} = \frac{-h''}{(1 + (h')^2)^{3/2}} \tag{36}$$

If the 3x3 stencil about cell (i,j) in (34) contains a third material, then $\kappa_{i+1/2,j}$ is approximated using central difference techniques:

Stencil contains rigid boundary Referring to Figure 11, if the 3x3 stencil contains a 3rd rigid material, $m = 3$, then we approximate the curvature $\kappa_{i,j}$ in (34) as follows:

$$\kappa_{i,j} = \nabla \cdot (H(\phi_3)\boldsymbol{n}_{ghost} + (1 - H(\phi_3))\boldsymbol{n}) \tag{37}$$

$$H(\phi_3)_{i+1/2,j+1/2} = \left\{ \begin{array}{cc} 0 & \phi_{3,i+i',j+j'} \le 0, \text{ all } i',j' = 0,1 \\ 1 & \text{otherwise} \end{array} \right. \tag{38}$$

$\boldsymbol{n}_{ghost}$ is defined as follows (see (Arienti and Sussman, 2014)):

$$\tilde{\phi} \equiv \frac{\phi_1 - \phi_2}{2}$$

$$\boldsymbol{n}_3 = -\frac{\nabla\phi_3}{|\nabla\phi_3|} \qquad \boldsymbol{n} = \frac{\nabla\tilde{\phi}}{|\nabla\tilde{\phi}|}$$

$$\boldsymbol{t}_1 = \boldsymbol{n}_3 \times \boldsymbol{n} \qquad \boldsymbol{t}_2 = \boldsymbol{n}_3 \times \boldsymbol{t}_1$$

$$\bar{\boldsymbol{n}}_{ghost} = \text{sign}(\boldsymbol{n}_3 \cdot \boldsymbol{t}_2)\sin(\theta)\frac{\boldsymbol{t}_2}{|\boldsymbol{t}_2|} - \cos(\theta)\boldsymbol{n} \qquad \boldsymbol{n}_{ghost} = \frac{\bar{\boldsymbol{n}}_{ghost}}{|\bar{\boldsymbol{n}}_{ghost}|}$$

Stencil contains 3rd fluid Referring to Figure 10, if the 3x3 stencil contains a 3rd fluid, $m = 3$, the distance functions, ϕ_1 and ϕ_2, are linearly interpolated to the 3x3 stencil centered at the point $(i + \theta, j)$ where,

$$\theta = \frac{|\tilde{\phi}_{i,j}|}{|\tilde{\phi}_{i,j}| + |\tilde{\phi}_{i+1,j}|} \qquad \tilde{\phi} \equiv \frac{\phi_1 - \phi_2}{2}. \tag{39}$$

Then we discretize the curvature using central differences,

$$\kappa_{i+1/2,j} = \frac{\gamma_1 \nabla \cdot \frac{\nabla \phi_1}{|\nabla \phi_1|} - \gamma_2 \nabla \cdot \frac{\nabla \phi_2}{|\nabla \phi_2|}}{\sigma_{12}},$$

where γ is defined in (6-7). $\nabla \phi$ is discretized at the nodes surrounding cell $(i + \theta, j)$; e.g.

$$(\phi_x)_{i+\theta+1/2,j+1/2} \approx \frac{\phi_{i+\theta+1,j} + \phi_{i+\theta+1,j+1} - \phi_{i+\theta,j} - \phi_{i+\theta,j+1}}{2\Delta x} \tag{40}$$

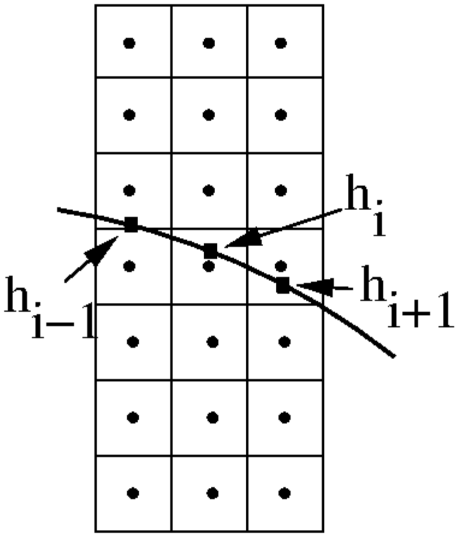

Figure 9: The level set height function method is used to approximate the curvature of the interface. The square symbols are located at the zero crossings of ϕ; e.g. $h_i = (1 - \theta_{i,j+1/2})y_j + \theta_{i,j+1/2}y_{j+1}$ where $\theta_{i,j+1/2} \equiv \frac{|\phi_{i,j}|}{|\phi_{i,j}|+|\phi_{i,j+1}|}$.

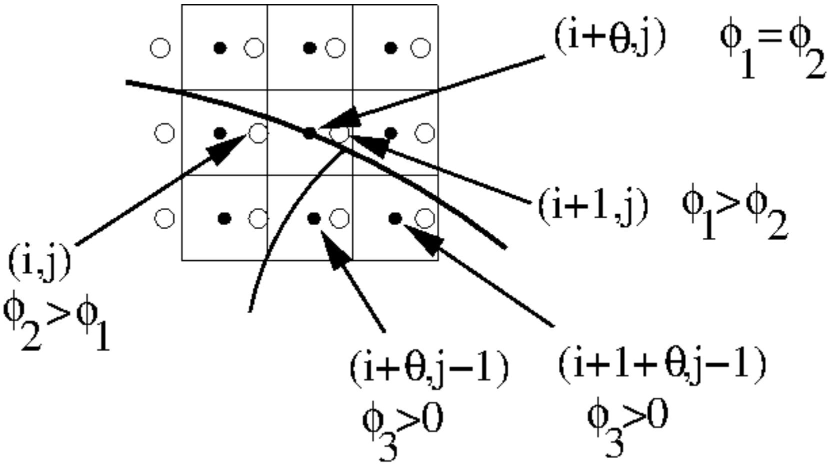

Figure 10: Illustration of the 3x3 stencil used to calculate the curvature $\kappa_{i+1/2,j}$ when the stencil contains a 3rd fluid material (material 3 in this diagram). $(i+\theta,j)$ is the $\Gamma_{1,2}$ interface crossing between cells (i,j) and $(i+1,j)$ $(\theta = |\tilde{\phi}_i|/(|\tilde{\phi}_i| + |\tilde{\phi}_{i+1}|)$, $\tilde{\phi} = (1/2)(\phi_1 - \phi_2))$. Given a 4x3 stencil of distance function values, $\phi_{i+i',j+j'}$, $i' = -1,\ldots,2$, $j' = -1,0,1$ (open circles), the distance functions are first interpolated to a 3x3 stencil (filled circles) centered at $(i+\theta,j)$. Then given the 3x3 stencil of values for the distance functions $\phi_{i+\theta+i',j+j'}$, $i' = -1,0,1$, $j' = -1,0,1$, the central difference curvature discretization technique is used (see (40)).

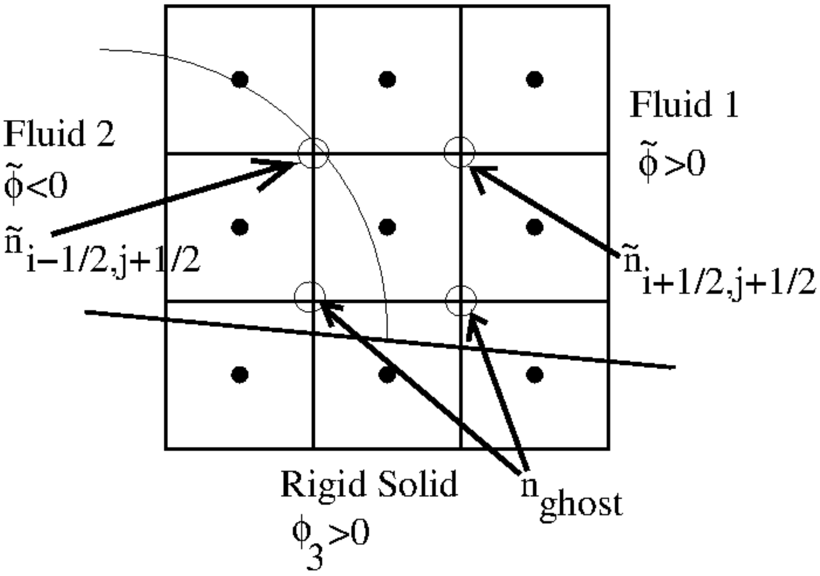

Figure 11: Illustration of the 3x3 stencil used to calculate the curvature κ_i when the stencil contains a rigid material (material 3). Given the 3x3 stencil of values for the distance function $\tilde{\phi}_{i+i',j+j'}$, $i' = -1, 0, 1$, $j' = -1, 0, 1$ ($\tilde{\phi} \equiv (1/2)(\phi_1 - \phi_2)$), the central difference curvature discretization technique is used (see (37)). ϕ_3 and $\tilde{\phi}$ are defined at the closed circles and the normals $\boldsymbol{n}_{ghost}$ and $\tilde{\boldsymbol{n}}$ are defined at the open circles.

3.6. Approximate projection method

Given the cell centered velocity field, $\boldsymbol{V}$,

$$\boldsymbol{V} = \boldsymbol{u}^{advect} + \Delta t \left(\boldsymbol{F}^{viscous} + \boldsymbol{F}^{tension} + \boldsymbol{g} \right)$$

we "approximately" project this velocity field onto the space of divergence free velocity fields.

1. Interpolate $\boldsymbol{V}$ from cell centers to cell faces,

$$\boldsymbol{V}^{MAC} = \mathcal{I}(\boldsymbol{V} - \boldsymbol{F}^{tension}) + \boldsymbol{F}^{MAC,tension} \tag{41}$$

where $\mathcal{I}$ is a momentum preserving interpolation operator (Kwatra et al., 2009; Jemison et al., 2014) and the discretized surface tension forces, $\boldsymbol{F}^{tension}$ and $\boldsymbol{F}^{MAC,tension}$, are defined above by equations (32) and (33).

2. Project $\boldsymbol{V}^{MAC}$ exactly onto the space of discretely divergence free velocity fields:

$$\boldsymbol{u}^{MAC,n+1} = \boldsymbol{V}^{MAC} - \Delta t \frac{\nabla p}{\rho^{n+1}} \tag{42}$$

$$\nabla \cdot \frac{\nabla p}{\rho^{n+1}} = \frac{\nabla \cdot \boldsymbol{V}^{MAC}}{\Delta t} \tag{43}$$

3. Interpolate the pressure p found in (43) from cell centers to face centers using the condition of constant contact (Kwatra et al., 2009; Jemison et al., 2014) and then update the new cell centered velocity:

$$\boldsymbol{u} = \boldsymbol{V} - \Delta t \frac{\nabla p^{MAC}}{\rho^{n+1}}. \tag{44}$$

Remarks:

- We call our method an "approximate projection method" (Almgren et al., 1996; Jemison et al., 2013) because, although the process of deriving $\boldsymbol{u}^{MAC,n+1}$ from $\boldsymbol{V}^{MAC}$ is an exact projection(Chorin, 1968; Bell et al., 1989), i.e.,

$$\boldsymbol{u}^{MAC,n+1} \equiv \mathcal{P}^{MAC}\boldsymbol{V}^{MAC} \quad \mathcal{P}^{MAC} = (\mathcal{P}^{MAC})^2 \quad \mathcal{P}^{MAC} \perp \mathcal{I} - \mathcal{P}^{MAC},$$

the process of deriving $\boldsymbol{u}^{n+1}$ from $\boldsymbol{V}$ is not an exact projection. In other words, if we implicitly define $\mathcal{P}$ as,

$$\boldsymbol{u}^{n+1} \equiv \mathcal{P}\boldsymbol{V},$$

it is not necessarily true that $\mathcal{P} = (\mathcal{P})^2$ or that $\mathcal{P} \perp \mathcal{I} - \mathcal{P}$.

- The interpolation operator $\mathcal{I}$ (41) is a mass weighted interpolation from cell control volumes to face control volumes. The cell, $\Omega_{i,j}$, is separated into left and right control volumes, e.g., $\Omega_{i,L}$ and $\Omega_{i,R}$ for interpolating the horizontal velocity. The interpolation of cell centered velocity to cell faces should respect conservation of momentum, so it is required that the integral over all face centered control volumes (45) be equal to the integral over all cells. We define the face control volume $\Omega_{i+1/2}$ as

  $$\Omega_{i+1/2} = \Omega_{i,R} \cup \Omega_{i+1,L} \tag{45}$$

  where $\Omega_{i,R}$ is the right half control volume of cell i and $\Omega_{i+1,L}$ is the left half control volume of cell $i+1$ as illustrated in Figure 12. The density over each half control volume is derived from the MOF linearly reconstructed interface:

  $$\rho_{i,R} = \frac{1}{|\Omega_{i,R}|} \sum_{m=1}^{M} |\Omega_{m,i} \cap \Omega_{i,R}|\rho_m \tag{46}$$

  $$\rho_{i+1,L} = \frac{1}{|\Omega_{i+1,L}|} \sum_{m=1}^{M} |\Omega_{m,i+1} \cap \Omega_{i+1,L}|\rho_m \tag{47}$$

  The face centered density $\rho_{i+1/2}$ is defined as the mass in the half-cell regions $\Omega_{i,R}$ and $\Omega_{i+1,L}$ divided by the volume of the face-centered control volume $\Omega_{i+1/2}$ (48),

  $$\rho_{i+1/2} = \frac{\rho_{i,R}|\Omega_{i,R}| + \rho_{i+1,L}|\Omega_{i+1,L}|}{|\Omega_{i+1/2}|}. \tag{48}$$

  The face centered velocity that is to be projected (41) is now defined as a mass-weighted interpolation of the cell centered velocity that is to be projected, e.g.,

  $$u_{i+1/2} = \frac{u_i\rho_{i,R}|\Omega_{i,R}| + u_{i+1}\rho_{i+1,L}|\Omega_{i+1,L}|}{\rho_{i+1/2}|\Omega_{i+1/2}|}. \tag{49}$$

- The finite volume method is used to discretize (43). For example,

$$(\nabla \cdot \boldsymbol{V}^{MAC})_{i,j} \approx \frac{u_{i+1/2,j} - u_{i-1/2,j}}{\Delta x} + \frac{v_{i,j+1/2} - v_{i,j-1/2}}{\Delta y}$$

$$(p_x/\rho)_{i+1/2,j} \approx \frac{p_{i+1,j} - p_{i,j}}{\rho_{i+1/2,j}\Delta x}$$

- The cell-averaged momentum is updated in a conservative fashion (44). It is required to interpolate the cell centered pressure to the cell faces. As in (Kwatra et al., 2009; Jemison et al., 2014), we define the momentum equation in each half cell region, $\Omega_{i,R}$ and $\Omega_{i+1,L}$:

$$\frac{Du_{i,R}}{Dt} = \frac{u_{i,R}^{n+1} - u_{i,R}^{*}}{\Delta t} = -\frac{p_{i+1/2} - p_i}{\rho_{i,R}\Delta x/2} \tag{50}$$

and

$$\frac{Du_{i+1,L}}{Dt} = \frac{u_{i+1,L}^{n+1} - u_{i+1,L}^{*}}{\Delta t} = -\frac{p_{i+1}^{n+1} - p_{i+1/2}^{n+1}}{\rho_{i+1,L}\Delta x/2}. \tag{51}$$

We apply the constraint that the interface between cells must remain in contact (Kwatra et al., 2009); i.e. $\frac{Du_{i,R}}{Dt} = \frac{Du_{i+1,L}}{Dt}$. Using this constraint and Equations (50 - 51), the pressure at the cell face $p_{i+1/2}$ (52) is found:

$$p_{i+1/2} = \frac{\rho_{i,R}p_{i+1} + \rho_{i+1,L}p_i}{\rho_{i,R} + \rho_{i+1,L}} \tag{52}$$

The derivations of the half cell densities, $\rho_{i,R}$ and $\rho_{i+1,L}$, are given by (46) and (47). With pressure defined at cell faces, we can conservatively update the cell-averaged momentum, e.g. for the horizontal velocity (53):

$$u_i^{n+1} = u_i^{*} - \Delta t \frac{p_{i+1/2}^{n+1} - p_{i-1/2}^{n+1}}{\rho_i \Delta x} \tag{53}$$

4. Results and discussion

The time step, Δt, is chosen according to the following scheme:

$$\Delta t = \min(\Delta t^{advect}, \Delta t^{tension}) \tag{54}$$

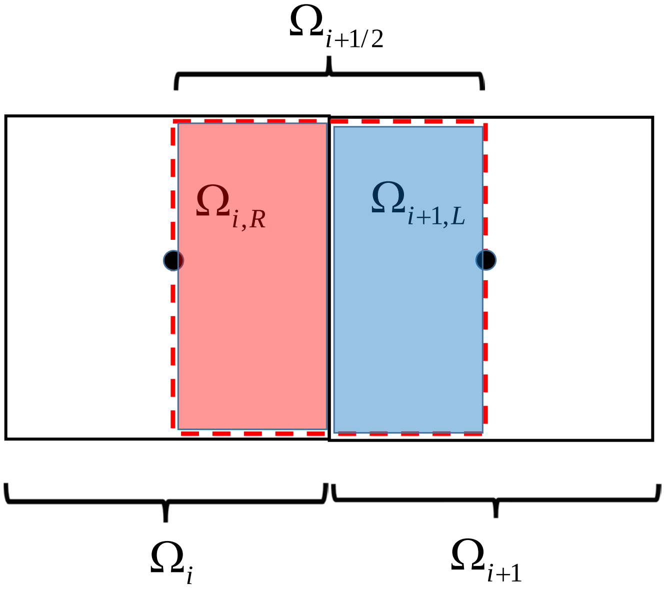

Figure 12: Left and right control volumes $\Omega_{i,R}$, $\Omega_{i+1,L}$, with face-centered control volume $\Omega_{i+1/2}$. Cell centers are shown as dots, and the boundary of the face-centered control volume is shown as dashes.

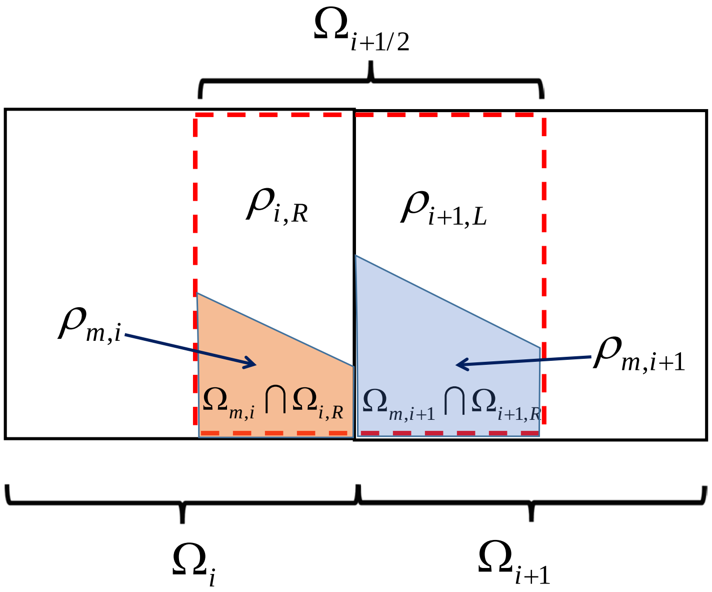

Figure 13: To compute the half cell densities $\rho_{i,R}$ and $\rho_{i+1,L}$ in cut cells, the MOF reconstructed interface is used to determine the half cell volume fractions Fm, i, R and $Fm, i+1, L$, so that one can derive $\rho_{i,R} = \sum_m F_{m,i,R}\rho_{m,i}$ and $\rho_{i+1,L} = \sum_m F_{m,i+1,L}\rho_{m,i+1}$.

$$\Delta t^{advect} = CFL \frac{\Delta x}{\max_{i,j} |u_{i,j}|} \tag{55}$$

$$\Delta t^{tension} = \min_{m,n} \frac{\Delta x^{3/2}}{\sqrt{\frac{2\pi\sigma_{m,n}}{\rho_m + \rho_n}}} \tag{56}$$

If the Weymouth and Yue (Weymouth and Yue, 2010) directionally split algorithm is used then,

$$CFL = \frac{1}{2\text{DIM}}, \tag{57}$$

where "DIM" is 2 or 3. If the Eulerian Implicit, Lagrangian Explicit (EI-LE (Aulisa et al., 2007; Scardovelli and Zaleski, 2003)) directionally split algorithm is used, then $CFL = 1/2$.

We use dynamic block structured adaptive mesh refinement in order to define the computational grid (Sussman et al., 1999; Sussman, 2005) (AMR). A computational domain that is organized using AMR is made up of a hierarchy of adaptive levels $\ell = 0, \ldots, \ell^{max}$ with each level being the union of disjoint rectangular grids. Level $\ell = 0$ is the coarsest level and the mesh size on each finer level is half the mesh size of the preceding level, $\Delta x^{\ell+1} = \Delta x^{\ell}/2$.

Referring to figure (14), filled circles represent cells or faces not hidden by a finer mesh. Open circles are either hidden coarse level cells or faces or fictitious fine grid cells. The solution at cells or faces corresponding to open circles are interpolated from the solution at cells or faces corresponding to filled circles. Coarse and fine levels are synchronized by "averaging down" the fine level solution onto the coarser level. For example, the hidden coarse grid cell value at cell "3" is the volume weighted average of the finer level cells "5," "6," "7," and "8." It could be that the stencil for the fine level cell "6" includes the fictitious fine level cell "9." In this case, the fictitious cell "9" value is interpolated from the coarse level values at cells "1," "2," "3," and "4." The algorithm used for interpolating volume fraction and moment data from coarse levels to fine levels, and the algorithm used for averaging down volume fraction and moment data from fine level cells to hidden coarse level cells is identical to that reported in (Jemison et al., 2013).

Momentum and pressure are interpolated from coarse to fine levels using piecewise constant interpolation. This is in contrast to our recent work in (Jemison et al., 2014), in which conservative minmod limited second order interpolation was used for momentum, and bilinear interpolation was used for interpolating pressure from the coarse grid to fine grid ghost cells. The reason we choose piecewise constant interpolation is because we find little difference in accuracy when computing the example calculations in this paper, and the piecewise constant interpolation for pressure leads to a symmetric matrix system for discretizing (43) which can be inverted quickly(Duffy et al., 2012). When piecewise constant interpolation is used for pressure, it is important that the gravitational force is expressed as,

$$\boldsymbol{F}^{gravity} = \nabla p_{hydro}(z), \qquad p_{hydro}(z) = gz \tag{58}$$

and then the gradient operator in (58) is discretized the same as that in (42) and (44).

We simulate the following cases using the proposed method to illustrate its robustness and accuracy. These test problems are: (1) severe 2D and 3D deformation of three materials in a prescribed deformational flow field, (2) relaxation to static shape for 2D droplet on a slope, (3) the liquid lens triple point problem, (4) downward liquid jets, (5) upward liquid jets, (6) Binary collision of two water drops (7) Binary collisions of a water drop and a diesel drop (8) droplet impingement onto a thin liquid film, and (9) droplet impingement onto a smooth solid wall.

4.1. Severe 2D and 3D multimaterial deformation in a prescribed deformational flow field

We first test our multimaterial reconstruction and advection algorithms for interface deformation in a prescribed flow field. In the results that follow we compare the computed solution to the exact solution using the symmetric difference error. We define Ω_C and Ω_E to be the computed and exact regions respectively of a deforming material in the domain. The symmetric difference error is then,

$$E_{sym} = |\Omega_C \cup \Omega_E - \Omega_C \cap \Omega_E|. \tag{59}$$

(59) can also be defined as,

$$E_{sym} = \sum_{i,j} \int_{\Omega_{i,j}} |H(\boldsymbol{n} \cdot (\boldsymbol{x} - \boldsymbol{x}_{i,j}) + b) - H(\phi_E(\boldsymbol{x}))| d\boldsymbol{x}. \tag{60}$$

H is the Heaviside function (5), $\boldsymbol{n}$ and b are derived from the interface reconstruction (12), $\boldsymbol{x}_{i,j}$ is the center of the cell $\Omega_{i,j}$, and the zero level set of $\phi_E(\boldsymbol{x})$ is the exact interface location.

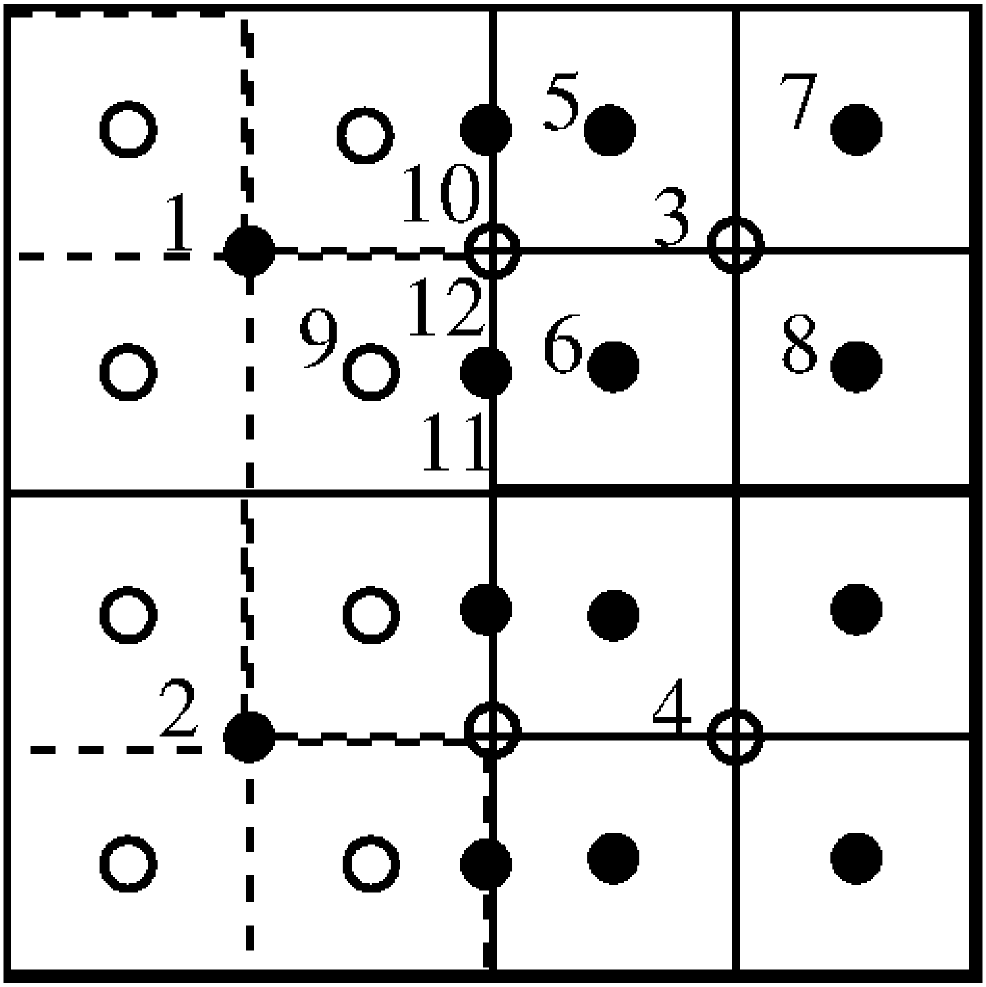

Figure 14: Illustration of a coarse/fine interface on an AMR grid. Filled circles represent cells or faces not hidden by a finer mesh. Open circles are either hidden coarse level cells or faces or fictitious fine grid cells.

We compute the symmetric difference error by approximating the integral in (60) using adaptive quadrature.

4.1.1. 2D Single Vortex

In this test, a circle of radius $R_0 = 0.15$ and center $(0.5, 0.75)$ is placed inside a unit sized box. The velocity field is given by the stream function

Bell et al. (1989):

$$\Psi(x, y, t) = \frac{1}{\pi}\sin^2(\pi x)\sin^2(\pi y)\cos(\frac{\pi t}{T}), \tag{61}$$

where $T = 8$ is the period of the reversing vortical flow.

The resulting velocity field first stretches the circle into an ever thinner filament that wraps around the center of the box, then after time $t = T/2$, slowly reverses and pulls the filament back into the initial circular shape at time $t = T$.

For this test we prescribe the velocity at the cell faces in terms of finite differences of the exact stream function Ψ (61).

In table 1, we compare the error at $t = T$ ($T = 8$), E_{sym} (59), for the following two cases: (i) Weymouth and Yue advection strategy(Weymouth and Yue, 2010) in which the initial circle is artificially cut in half along the vertical axis, and (ii) alternating EI-LE advection strategy(Aulisa et al., 2007; Scardovelli and Zaleski, 2003) also in which the initial circle is artificially cut in half along the vertical axis.

The results using the Weymouth and Yue advection strategy on a 512 × 512 grid is illustrated in Figures 15 and 16. For comparison purposes we also show the results for the deformation of the circle in which the initial circle is not artificially cut in half. We note that both advection strategies give comparable errors on the finest mesh, but the alternating EI-LE strategy is twice as fast since the CFL condition is more lenient than that for the Weymouth and Yue advection strategy. We also note that as the grid is refined, the error for the 3 material deformation problem approaches the error of the 2 material case.

Size	3 material Weymouth and Yue	3 material EI-LE	2 material Weymouth and Yue
128	$7.6E-3$	$2.4E-3$	$1.0E-3$
256	$1.4E-3$	$6.4E-4$	$7.1E-5$
512	$3.2E-5$	$3.2E-5$	$1.8E-5$

Table 1: Symmetric Difference Error from Section 4.1.1, for the reversible $2D$ vortex. Errors are taken at the end time $t = T$.

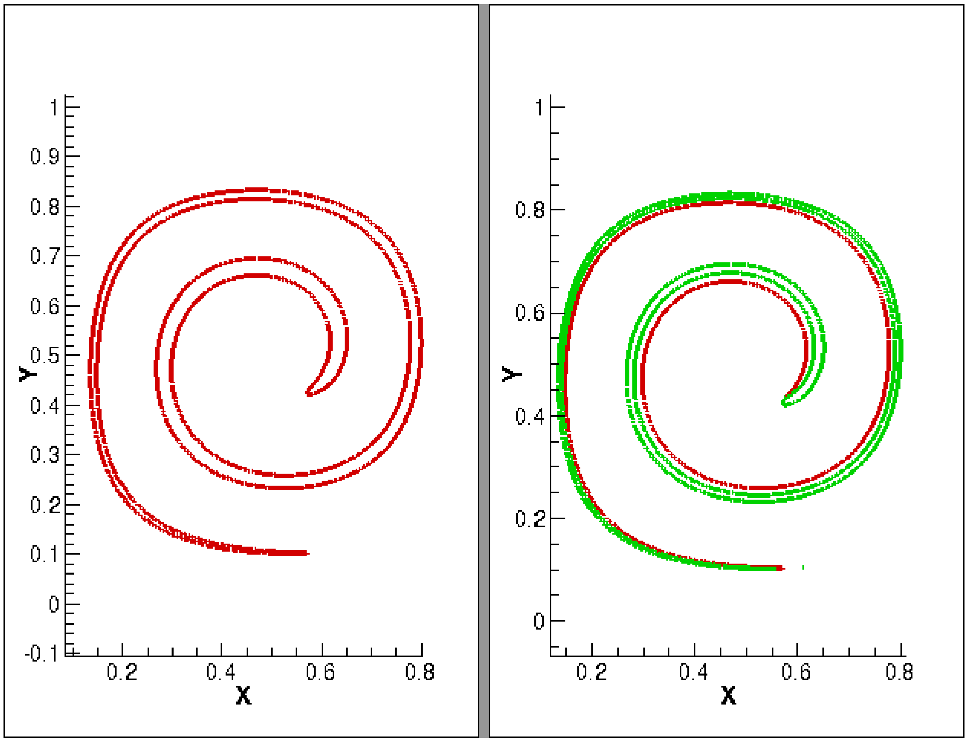

Figure 15: Deformation problem with period $T = 8$. Results at $t = 4.0$. LEFT: 2 materials. RIGHT: 3 materials. The corresponding piecewise linear reconstructed interface is plotted. Base grid 64x64. three levels of AMR; effective fine grid resolution 512x512.

4.2. Reversible Vortex - 3D

In this test problem, a sphere with radius 0.15 and center $(0.35, 0.35, 0.35)$ is placed in the following flow field:

$$u = 2\cos(\pi t/3)\sin^2(\pi x)\sin(2\pi y)\sin(2\pi z) \tag{62}$$

$$v = -\cos(\pi t/3)\sin^2(\pi y)\sin(2\pi x)\sin(2\pi z) \tag{63}$$

$$w = -\cos(\pi t/3)\sin^2(\pi z)\sin(2\pi x)\sin(2\pi y) \tag{64}$$

The initial sphere undergoes severe deformation for $0 < t < 3/2$. For $3/2 < t < 3$, the flow is “reversed” and the final expected shape is a sphere again.

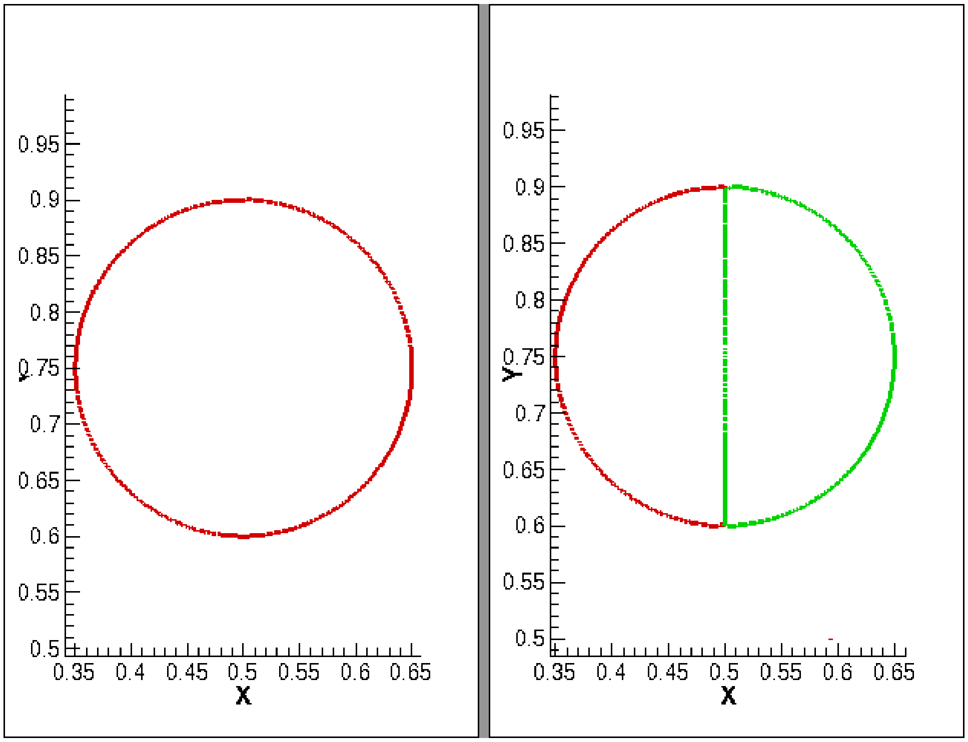

Figure 16: Deformation problem with period $T = 8$. Results at $t = 8.0$. LEFT: 2 materials. RIGHT: 3 materials. The corresponding piecewise linear reconstructed interface is plotted. Base grid 64x64. three levels of AMR; effective fine grid resolution 512x512.

In table 2, we compare the error at $t = 3$, E_{sym} (59), for the following two cases: (i) Weymouth and Yue advection strategy(Weymouth and Yue, 2010) in which the initial sphere is artificially cut in half along the vertical axis, and (ii) alternating EI-LE-EI advection strategy(Aulisa et al., 2007; Scardovelli and Zaleski, 2003) also in which the initial sphere is artificially cut in half along the vertical axis.

The results using the alternating EI-LE-EI advection strategy on a $64 \times 64 \times 64$ grid are illustrated in in Figures 17 and 18. For comparison purposes we also show the results for the deformation of the sphere in which the initial sphere is not artificially cut in half.

Size	3 material Weymouth and Yue	3 material EI-LE-EI	2 material EI-LE-EI
32	$6.5E-3$	$5.6E-3$	$4.7E-3$
64	$2.1E-3$	$1.8E-3$	$2.0E-3$

Table 2: Symmetric Difference Error from Section 4.2, for the reversible $3D$ vortex. Errors are taken at the end time $t = 3$.

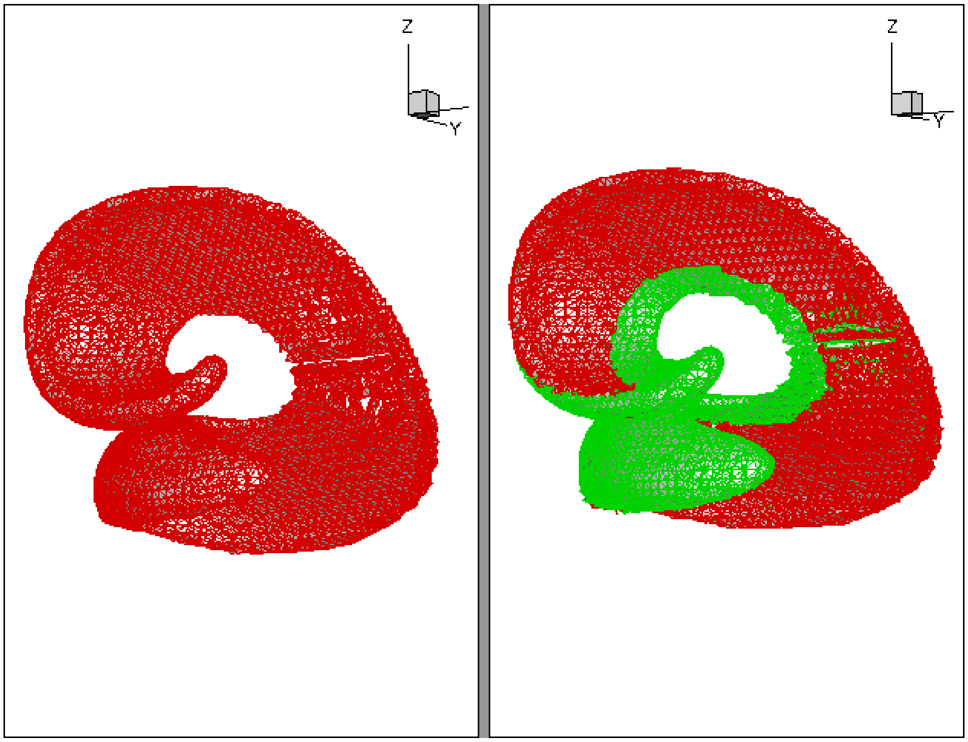

Figure 17: 3D Deformation problem with period $T = 3$. Results at $t = 1.5$. LEFT: 2 materials. RIGHT: 3 materials. The corresponding piecewise planar reconstructed interface is plotted. 64x64x64 grid.

4.3. 2D droplet on a slope

As in (Arienti and Sussman, 2014; Noel et al., 2012), we tested our MOF algorithm by performing a convergence study for the relaxation of a two-dimensional water droplet in gas on an 18^0 inclined solid plane. See Figure

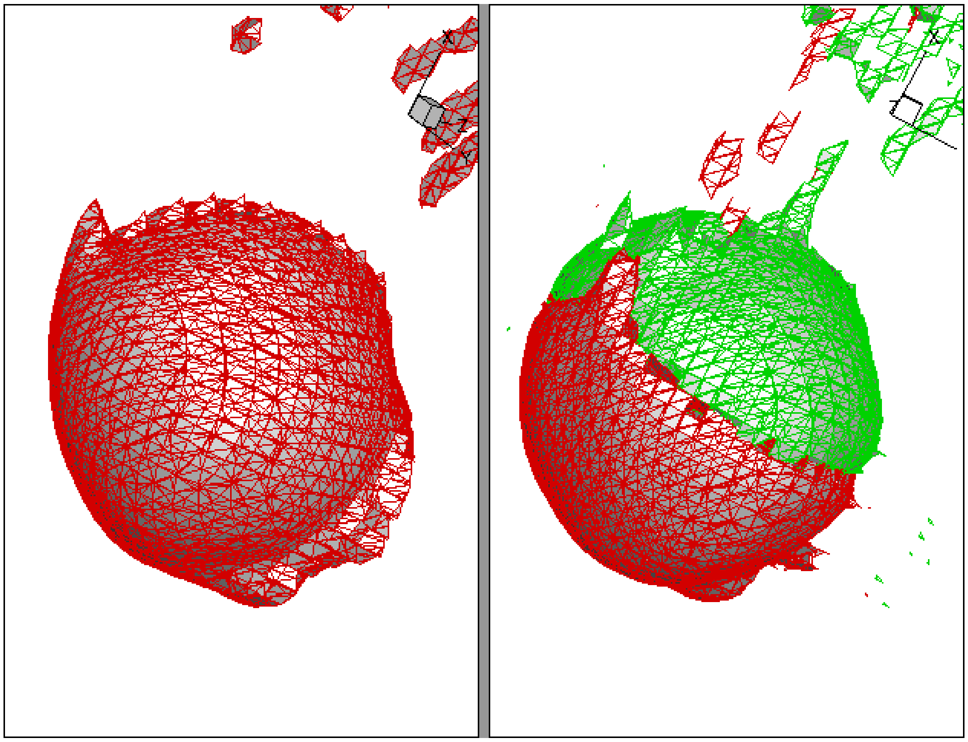

Figure 18: 3D Deformation problem with period $T = 3$. Results at $t = 3.0$. LEFT: 2 materials. RIGHT: 3 materials. The corresponding piecewise planar reconstructed interface is plotted. 64x64x64 grid.

19. There is no gravity. The inclined plane is defined as,

$$\Omega_{plane} = \{(x, y) | \tan(18^0)(x - 3) + 1 - y > 0\}. \tag{65}$$

The initial droplet is prescribed so that the initial contact angle is 90^0. The initial droplet shape is defined as,

$$\Omega_{drop} = \{(x, y) | 1 - ((x - 3)^2 + (y - 1)^2) > 0\} \cap \Omega^C_{plane} \tag{66}$$

The dimensionless parameters are: $\rho_1 = 1$, $\rho_2 = 0.0013$, $\mu_1 = 0.16$, $\mu_2 = 0.0025$, $\sigma_{12} = 1118.0$, $\sigma_{13} = 559.0$, and $\sigma_{23} = 1118.0$. These parameters are non-dimensionalized by the initial droplet radius $r_0 = 0.06348 cm$ (see Figure 19) and a characteristic velocity $U = 1 cm/s$. Material "1" corresponds to water (red), "2" corresponds to air (white), and "3" corresponds to solid (blue). The values of σ_{ij} correspond to a contact angle of 60^0.

The expected drop height is,

$$e_0 = (1 + \cos(\pi - \theta))R_\theta, \tag{67}$$

and the expected base length is

$$L_0 = 2\sin(\pi - \theta)R_\theta, \tag{68}$$

where R_θ is the final radius,

$$R_\theta = \sqrt{\frac{\pi}{2\theta - \sin(2\theta)}}R_0. \tag{69}$$

In table 3, we give the percent error for e_0 and L_0 when computed on successively refined grids.

Table 3: Percent error for the relaxation of a water drop on a sloped incline from a 90^0 contact angle to a 60^0 contact angle. The computational domain is 6x3 in dimensionless units. The computational grid is a hierarchy of adaptive, dynamic, rectangular grids with a base coarse grid of 96x48 grid cells. The error is checked for 3 different grid resolutions.

Levels	$100\frac{\lvert e_0 - e_0^{exact}\rvert}{e_0^{exact}}$	$100\frac{\lvert L_0 - L_0^{exact}\rvert}{L_0^{exact}}$
1	3.4	4.0
2	0.9	1.4
3	0.4	0.3

4.4. Liquid Lens test problem

We repeat the Liquid Lens test problem as in (Kim, 2007) (section 4.4 of (Kim, 2007)). Initially there are 3 materials with material 2 occupying a circle of diameter 0.3 in the center of the domain, material 1 occupying the remaining top half of the computational domain, and material 3 occupying the remaining bottom half of the computational domain. All 3 materials have the same unit density and share the same viscosity of 1/60. The surface tension coefficient between materials one and two and between materials two and three was set to $\sigma_{12} = 2/45$ and $\sigma_{23} = 2/45$ respectively. We tested our algorithm for four different values of the surface tension between materials one and three (σ_{13}): $\sigma_{13} = 3/90$, 4/90, 5/90, and 6/90. The expected steady

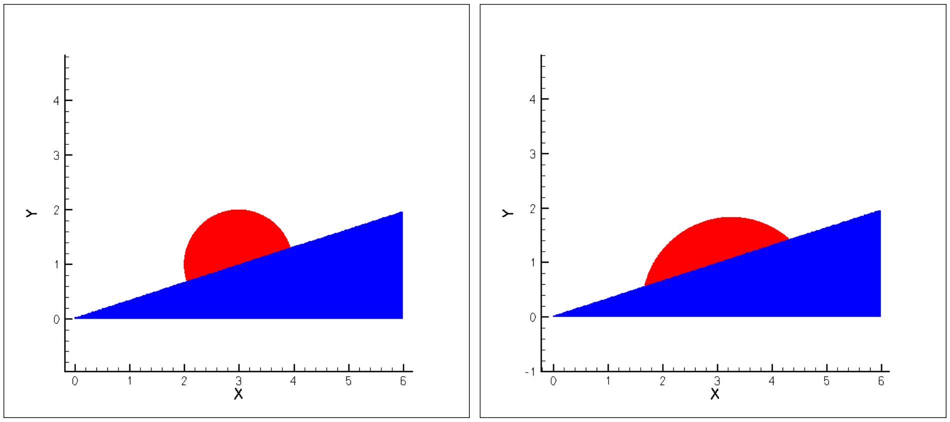

Figure 19: Relaxation of droplet (red) on a slope (blue) from 90^0 contact angle to 60^0 contact angle. Base coarse grid is a rectangular 96x48 grid. Effective fine grid resolution is 384x192. Left: initial conditions, Right: droplet at final static shape $t = 0.8$.

state solution has material 2 being stretched into a lens shape with major axis length of $L_0^{exact} = 0.381$, 0.416, 0.460, and 0.522 for the four cases of σ_{13}. In Figure 20 we illustrate the initial and steady state interfaces that we compute using our multimaterial MOF method for the case when $\sigma_{13} = 5/90$. In Table 4, we give the percent error in major axis length for the four different cases of σ_{13}. In all of our test cases, the volume fluctuated by less than 0.001 percent throughout the simulations.

4.5. Downward liquid jets

We study a downward liquid jet from a 3D round nozzle. Fig. 21 illustrates the geometry of the nozzle and the computational conditions. The geometry of the nozzle can be defined by the nozzle diameter D and nozzle height H_n. Uniform flow velocity is assigned at the nozzle inlet. Nonslip boundary condition is applied at the nozzle walls and top surface. Outflow boundary condition is applied on the rest boundaries.

The following fluid properties are used: water density $\rho_l = 1.0\times 10^3$ kg/m^3 , air density $\rho_g = 1.225$ kg/m^3 , water viscosity $\mu_l = 1.3 \times 10^{-3}$ kg/m.s , air viscosity $\mu_g = 2.0 \times 10^{-5}$ kg/m.s, surface tension $\sigma = 7.28 \times 10^{-2}$ kg/s^2 and the gravitational acceleration $g = 9.8$ m/s^2.

In the simulation the nozzle diameter D is 0.4 cm and the nozzle height H_n is 0.6 cm. Two levels of adaptive mesh refinement are used, resulting in

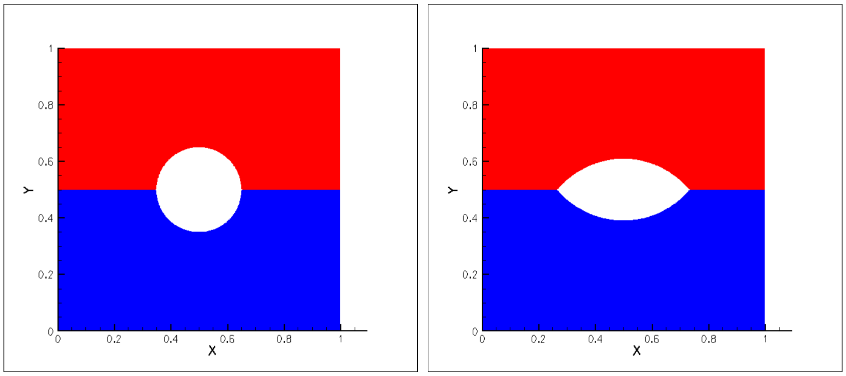

Figure 20: Stretching of a liquid lens. Red region indicates material 1, white region is material 2 and blue region is material 3. All materials have the same constant viscosity $\mu = 1/60$. $\sigma_{12} = 2/45$, $\sigma_{13} = 1/18$, and $\sigma_{23} = 2/45$. The computational domain dimensions are 1x1. The base coarse grid is a rectangular 64x64 grid. Effective fine grid resolution is 256x256. Left: initial conditions, Right: liquid lens at $t = 6$.

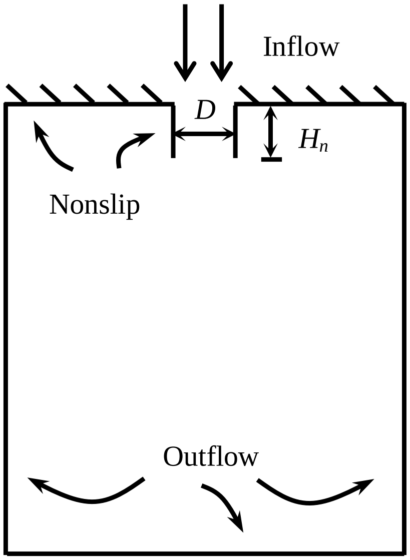

Figure 21: Illustration of nozzle geometry and computational domain for a downward jet. D is the nozzle diameter and H_n is the nozzle height.

Table 4: Percent error for the stretching of a liquid lens at static shape. Initially material 2 is a circle centered at $(1/2, 1/2)$, material 1 occupies the remaining top half, and material 3 occupies the remaining bottom half. The density and viscosity is constant for all three materials: $\rho = 1$, $\mu = 1/60$. The surface tension coefficients are $\sigma_{12} = 2/45$, $\sigma_{23} = 2/45$, and $\sigma_{13} = 3/90$, 4/90, 5/90, and 6/90. The computational domain dimensions are 1x1. The computational grid is a hierarchy of adaptive, dynamic, rectangular grids with a base coarse grid of 64x64 grid cells and two levels of refinement.

σ_{13}	L_0	L_0^{exact}	$100\frac{\lvert L_0 - L_0^{exact}\rvert}{L_0^{exact}}$
3/90	0.374	0.381	1.8%
4/90	0.407	0.416	2.2%
5/90	0.463	0.460	0.7%
6/90	0.531	0.522	1.7%

a mesh which has 12 grid points per nozzle diameter.

When the flow rate is lower, jet behavior is dominated by the gravitational force and the surface tension force. Dripping regime will occur if the gravitational force is larger than the surface tension force. Fig. 22 shows the time evolution of the dripping regime at a low nozzle inlet velocity of $v_0 = 6.0$ cm/s; When the flow rate is higher, the jet behavior is dominated by the inertial force and surface tension force, which leads to the jetting regime. Fig. 23 shows the time evolution of the jetting regime at a high nozzle inlet velocity of $v_0 = 20.0$ cm/s.

For purpose of generality, we introduce three non-dimensional parameters: the Reynolds number, the Weber number and the Ohnesorge number. The Reynolds number, $Re = \rho v_0 D/\mu$, gives a measure of the ratio of inertial forces to viscous forces. The Weber number, $We = \rho v_0^2 D/\sigma$, represents the relative importance of inertia and surface tension. The Ohnesorge number, $Oh = \sqrt{We}/Re = \mu/\sqrt{\rho\sigma D}$, relates viscous forces to the inertial and surface tension forces.

For the studied high inlet velocity case, the Reynolds number is 307, the Weber number is 1.1 and the Ohnesorge number is 0.0034. The small Ohnesorge number means that the viscous forces are less important than the inertial force and surface tension. The breakup length, which is defined as the distance between the nozzle tip and the point just before the first drop of

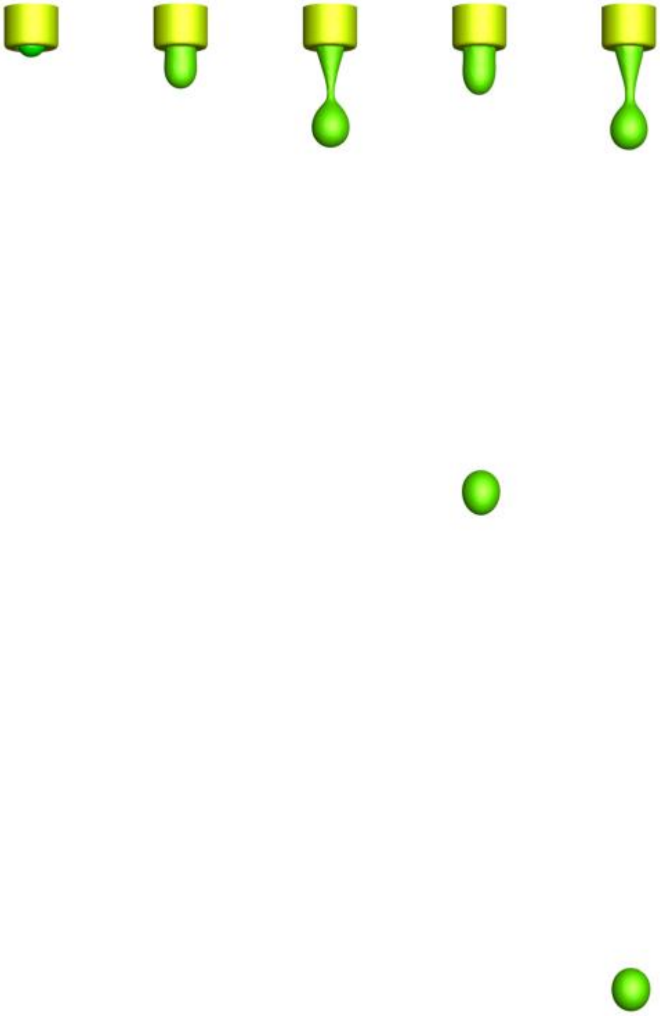

Figure 22: Snapshots of jet interface with a low velocity of $v_0 = 6.0$ cm/s.

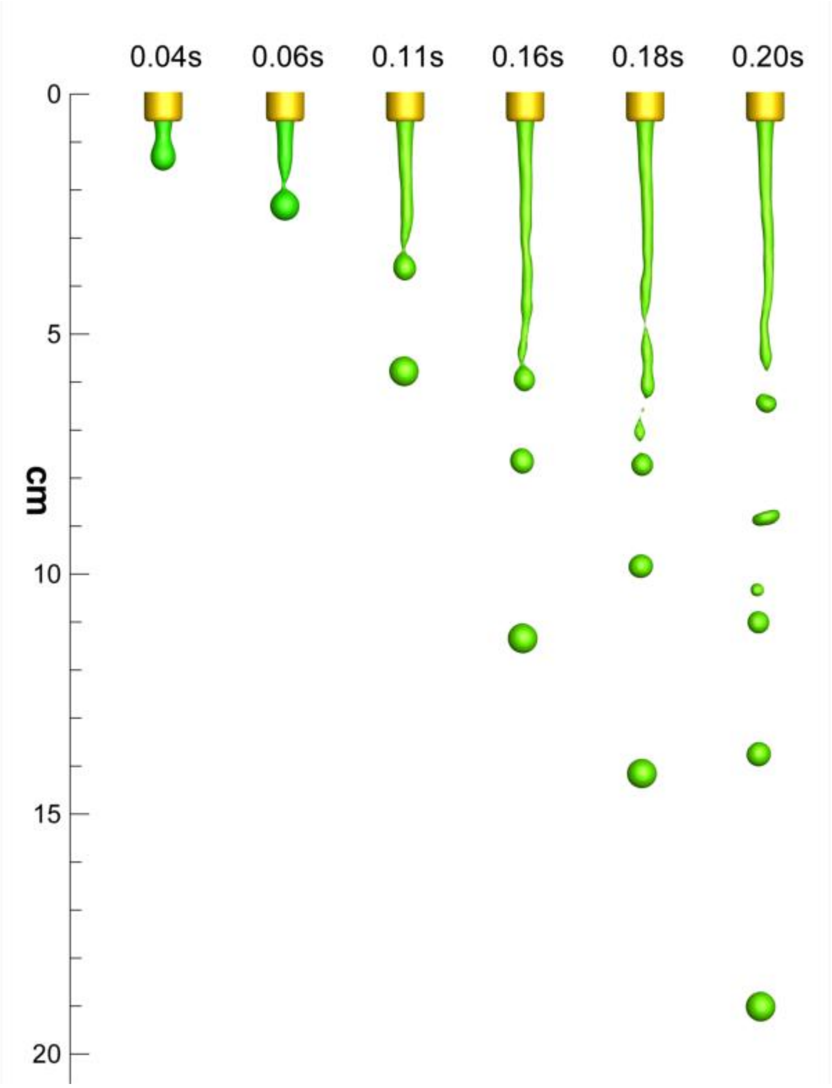

Figure 23: Snapshots of jet interface with a high velocity of $v_0 = 20.0$ cm/s.

the liquid jet, can be computed using the following formula (Ashgriz, 2011):

$$\frac{L}{D} = 1.04C\sqrt{We} \tag{70}$$

where L is the jet breakup length, and C is an empirical parameter. (Grant and Middleman, 1966) suggested the value of $C = 13$ based on experimental data for Rayleigh breakup of low viscosity jets.

The computed breakup length, as shown in Fig. 23, is about 6 cm and it is very close to the value of 5.7 cm using Eq. 70.

4.6. Upward liquid jets

We simulate upward liquid jet based on a geometry shown in Fig. 24. In Fig. 24 S_{LOW} and S_{UP} represent the lower and upper section of the nozzle outlet respectively. Two different nozzle configurations are used in our simulations. In the first case, both upper and lower surfaces are circles with the same diameter of 3.2 mm. In the second case, the lower surface is a circle but the upper surface is an ellipse which has the same cross sectional area as the lower surface and the ratio of its major axis and minor axis is 3. The nozzle has an inlet of diameter (D) of 17.4 mm, a wall thickness H_1 of 3 mm, and a height H_2 of 9.4 mm. Three levels of adaptive mesh refinement are used for these cases and the effective grid size is about $D_1/10$. i.e., 10 grid points per nozzle outlet diameter. The physical properties of the liquid and air are the same as that in the downward jet example.

In the first case, a uniform velocity $v_0 = 4.0$ cm is applied at the nozzle inlet. Fig. 25 shows the jet interface evolution with time. The maximum jet height is 14 cm. The jet height first increase, reach the maximum height and then decrease with water accumulating at the jet tip because of the gravity effect.

In the second case the same nozzle inlet velocity of 4.0 cm/s is applied. Fig. 26 shows the jet interface evolution. It is noticed that after leaving the nozzle, the major axis and minor axis of the jet switch. This phenomenon was discussed by (Lin, 2003) who argued that this switch is due to the effect of surface tension, which causes the jet section vibration about a equilibrium circle shape.

4.7. Binary collisions of two water drops

Binary collisions of liquid drops have been experimentally studied by (Ashgriz and Poo, 1990) and (Orme, 1997) and numerically studied by (Tanguy and Berlemont, 2005), (Chen and Yang, 2014), and (Nikolopoulos et al.,

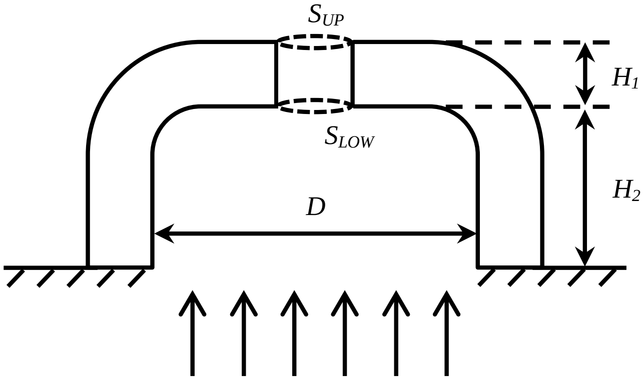

Figure 24: Illustration of nozzle geometry for upward jet. S_{UP} is the upper section of nozzle outlet, S_{LOW} is the lower section of nozzle outlet, D is the diameter of nozzle inlet, H_1 is the nozzle wall thickness and H_2 is the nozzle height.

Figure 25: Snapshots of upward liquid jet. A round nozzle is used.

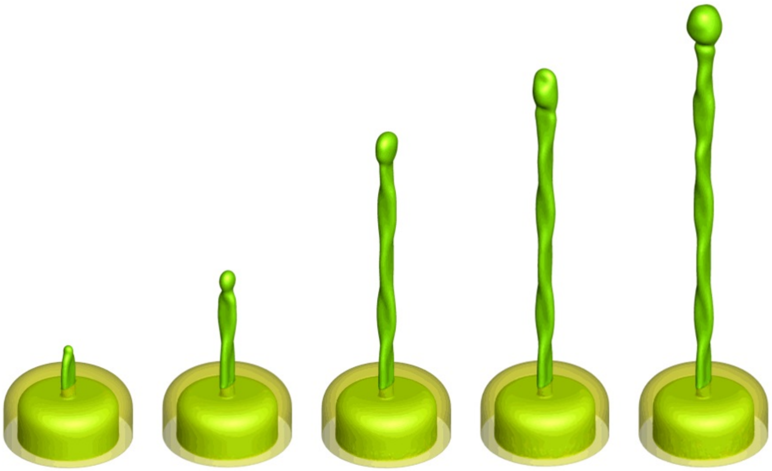

Figure 26: Snapshots of upward liquid jet. The nozzle has a round low surface and an elliptical top surface

2009). For equal sized head-on collisions the outcomes depend on the Reynolds number, Weber number which are defined as follows:

$$Re = \frac{\rho d u}{\mu} \qquad We = \frac{\rho d u^2}{\sigma}$$

where ρ and μ are the liquid density and viscosity, respectively, d is the drop diameter, u is the relative velocity of the two drops, and σ is the liquid surface tension. With the Reynolds number in the range of 500 and 4000, Ashgriz and Poo found that the Reynolds number did not play a significant role on the outcome (Ashgriz and Poo, 1990). In Figure 27, we show results of the simulation of the head-on collision of two equal sized water drops at the Weber number of 25, 40 and 96. In the experiments, it was found that reflexive separation occurs for a Weber number greater than nineteen and coalescence or bouncing occurs for a Weber number less than twenty. Our numerical results (Figure 27) corroborate these results.

4.8. Binary collisions of one water drop and one diesel drop

In Figure 28, we show results of the collision of a diesel oil drop with a water drop. These results can be compared with the experimental results reported by (Chen and Chen, 2006). As with the case for the collision of two water drops, again we have agreement between simulation and experiment for capturing the Weber number cutoff separating the coalescence regime from the reflexive separation regime.

4.9. Impingement of droplet on a thin liquid film

The complex phenomenon of droplet impingement on a thin film phenomenon is characterized by the Reynolds number Re, the Weber number We, the Ohnesorge number Oh and the nondimensional film thickness H defined as follows:

$$\begin{aligned} Re &= \rho v_0 D/\mu \\ We &= \rho v_0^2 D/\sigma \\ Oh &= \mu/\sqrt{\rho\sigma D} \\ H &= h/D \end{aligned} \tag{71}$$

where v_0 is the impact velocity, D is the droplet diameter and h is the film thickness. Also, a nondimensional time $T = tv_0/D$ is introduced and it is set to zero at the first contact between the droplet and the film.

At high We numbers, a crown structure is formed on the film surface and liquid jets or secondary droplets are splashed from the crown rim. This is called the splashing regime. At low We numbers, the droplet may deposit on the film surface without secondary droplets. This is called the deposition regime. The critical We number separating the splashing regime and the deposition regime is studied by many researchers (Cossali et al., 1997; Okawa et al., 2006). Two Weber numbers are simulated: $We = 100$ which corresponds to the deposition regime and $We = 600$ which corresponds to the splashing regime.

Fig. 29 shows the time evolution of the deposition process and Fig. 30 shows the splashing process. The effective grid size is about $D/70$ for the deposition case and $D/135$ for the splashing case. Different Rieber (Rieber and Frohn, 1999) who introduced random disturbance in his simulation, no random disturbance was introduced in our simulation. The initial distance from the droplet to the film is $0.13D$. For the deposition regime, as shown in Fig. 29, a crown-like structure is formed at the first stage of the impact. This crown-like structure travels outwards with a maximum crown height of $0.5D$ without any secondary droplet splashing. For the splashing regime, as shown in Fig. 30, fingers are formed at the top of crown rim. These fingers are then breakup into secondary droplets due to Rayleigh instability.

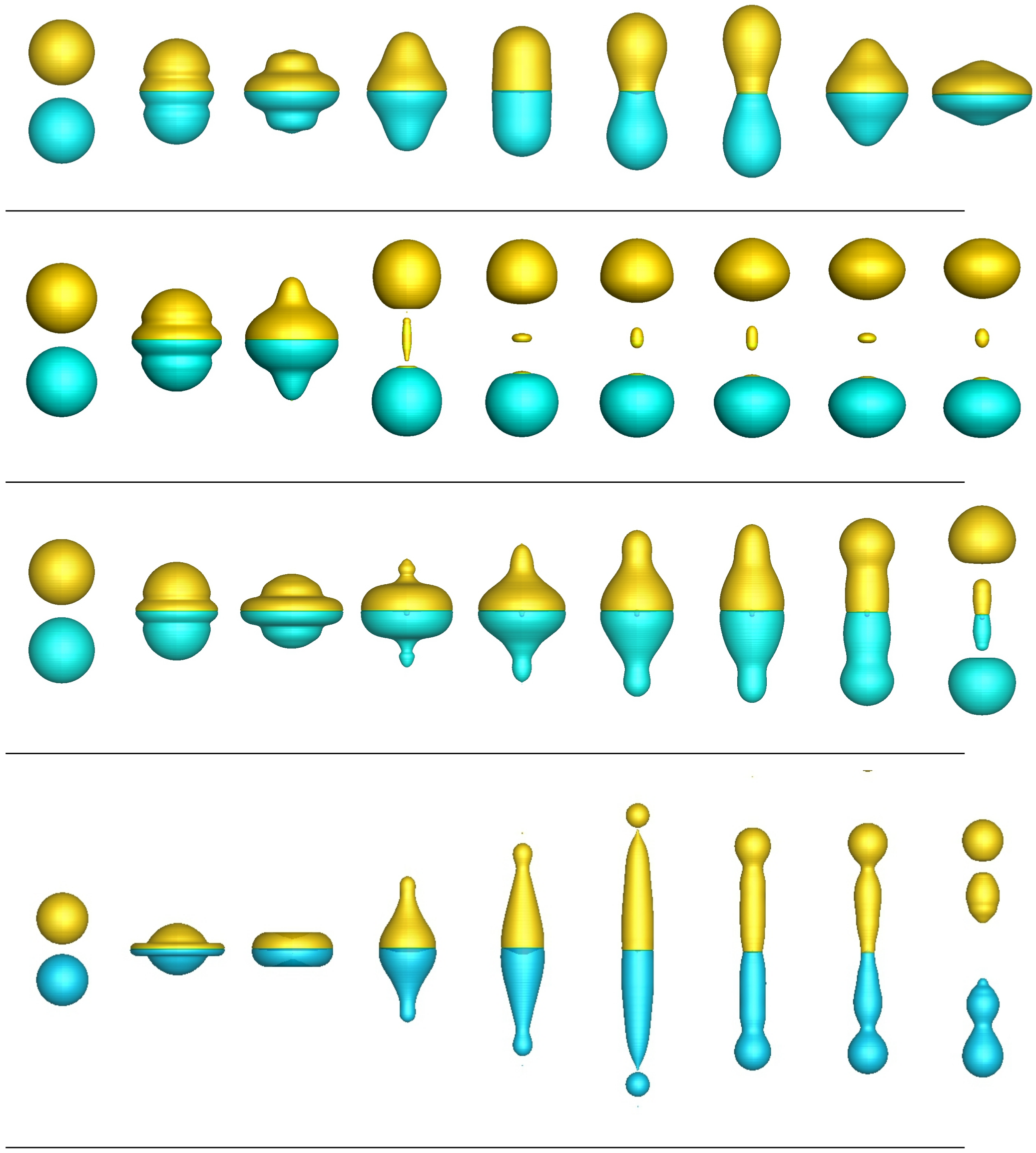

Figure 27: Numerical simulation of head-on collision of two water drops. From top to bottom Weber Number is 15, 25, 40, and 96, respectively. The computational grid is a block structured mesh with 16 cell per initial drop radius. One grid refinement is used(effective fine grid resolution is 32 cells per initial drop radius). Results are in agreement with experiments (Ashgriz and Poo, 1990). We capture the correct transition point for reflexive separation.

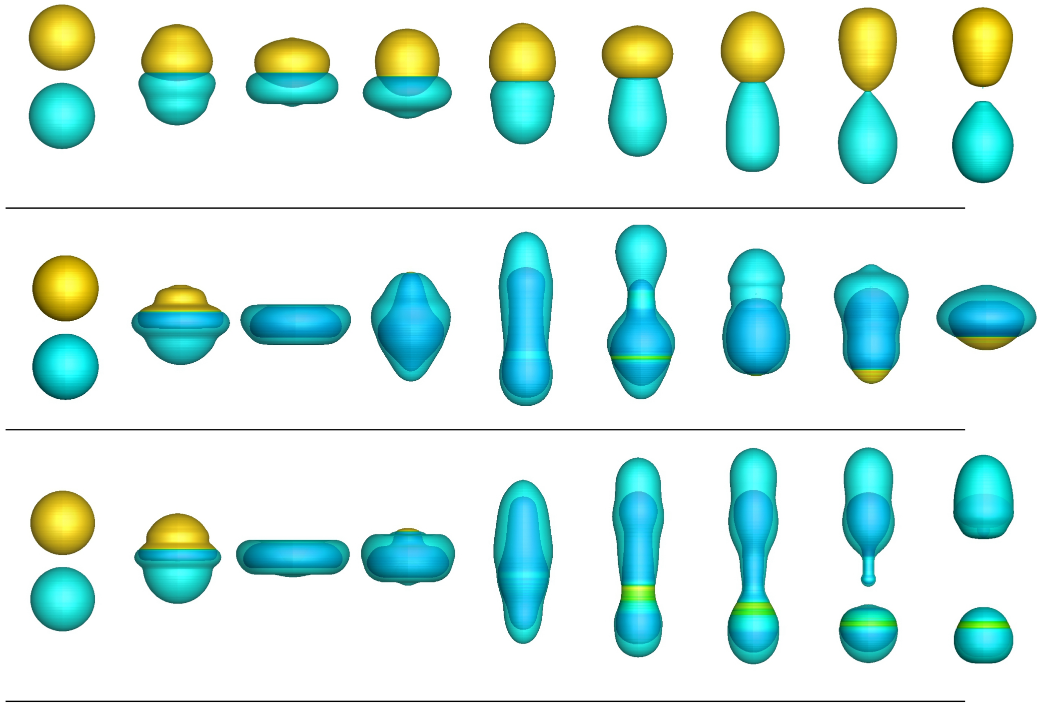

Figure 28: Numerical simulation of head-on collision of a diesel oil drop (cyan) with a water drop (gold) and resulting encapsulation. Weber Number equals 9.6, 45.3, and 58.9 for the top, middle and bottom rows respectively. Dimensionless drop diameter is 1 and computational domain size is $0 < r < 1.3$, $-3.9 < z < 3.9$. The computational grid is a block structured dynamic adaptive mesh with 48x288 coarse grid cells and 2 additional levels of adaptivity (effective fine grid resolution is 192x1152). Results are in agreement with experiments (Chen and Chen, 2006). We capture the correct transition point for reflexive separation. Simulations are done in 3d axisymmetric (RZ) coordinate system.

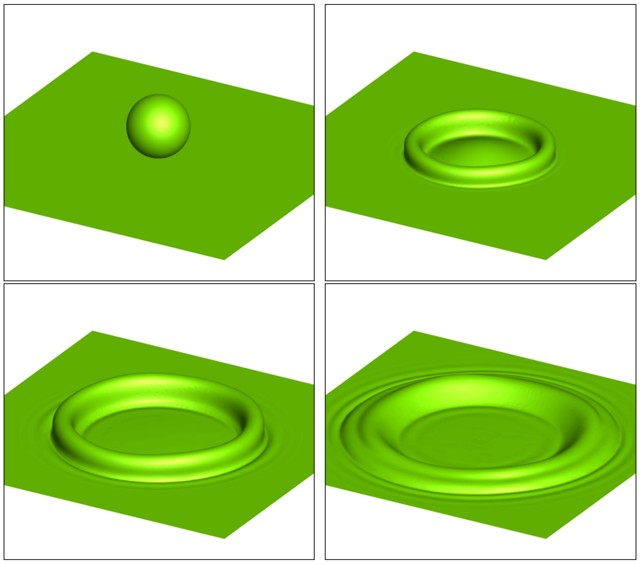

Figure 29: Snapshot of droplet-liquid film impingement, $We = 100$. From left to right, top to bottom: $T = 0.0$, $T = 1.0$, $T = 2.0$, and $T = 3.0$

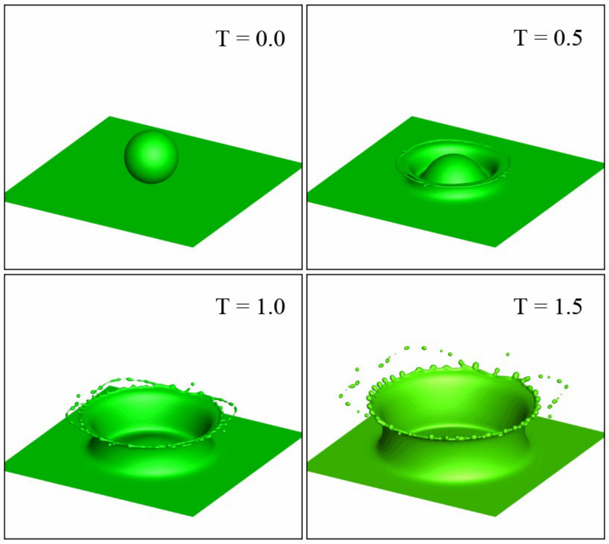

Figure 30: Snapshot of droplet-liquid film impingement, $We = 600$.

4.10. Impingement of droplet onto a solid wall

The impingement of a droplet on a smooth solid wall can result in different regimes such as spreading, splashing, receding and rebounding (Yarin, 2006). The Weber number, Ohnesorge number as well as the contact angle play an important role in the impact dynamics. We choose the droplet diameter $D = 3.6$ mm, density $\rho = 1.0 \times 10^3$ kg/m^3, viscosity $\mu = 8.67 \times 10^{-4}$ kg/m.s, surface tension $\sigma = 7.17 \times 10^{-2}$ kg/s^2 and impact velocity $v_0 = 0.77$ m/s, which correspond to $We = 30$ and $Oh = 0.0017$. A dynamic contact angle model from (Jiang et al., 1979) is used, and the equilibrium contact angle is set to 87°. Two levels of grid adaptation are used and the effective grid size is $D/72$.

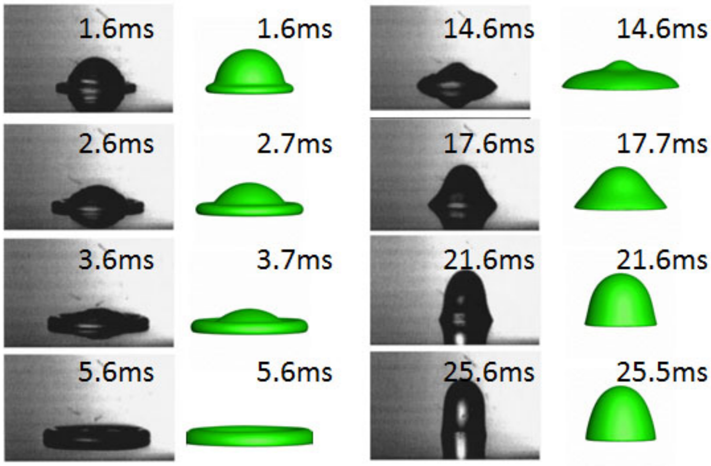

Figure 31: Droplet impinging on a solid wall. Left, experimental results from (Kim and Chun, 2001). Right, present numerical results.

Figure 31 shows the evolution of the droplet shape. The computed droplet shape is also compared with experimental data from Kim and Chun(Kim and Chun, 2001). As can be seen from Fig. 31, the experimental results and the numerical results are in good agreement.

5. Concluding remarks

A new method was presented to study incompressible flows involving more than two materials. In this method, the MOF interface reconstruction method was used to capture the material interfaces. The directionally split cell integrated semi-Lagrangian method was used to advect interfaces and momentum. The block structured adaptive mesh refinement was used to increase the resolution near material interfaces. Various 2D, 3D axisymmetric and 3D problems were simulated. Comparisons were made with analytical or experimental results. Our simulation showed that the proposed method is able to simulate multiphase problems involving more than two materials. The method is also able to capture the contact line dynamics and triple junctions.

References

Ahn, H. T., Shashkov, M., 2007. Multi-material interface reconstruction on generalized polyhedral meshes. Journal of Computational Physics 226 (2), 2096–2132.

Ahn, H. T., Shashkov, M., 2009. Adaptive moment-of-fluid method. Journal of Computational Physics 228 (8), 2792–2821.

Ahn, H. T., Shashkov, M., Christon, M. A., 2009. The moment-of-fluid method in action. Communications in Numerical Methods in Engineering 25 (10), 1009–1018.

Almgren, A. S., Bell, J. B., Szymczak, W. G., 1996. A numerical method for the incompressible navier-stokes equations based on an approximate projection. SIAM Journal on Scientific Computing 17 (2), 358–369.

Arienti, M., Sussman, M., 2014. An embedded level set method for sharp-interface multiphase simulations of diesel injectors. International Journal of Multiphase Flow 59, 1–14.

Ashgriz, N., 2011. Handbook of atomization and sprays. Springer.

Ashgriz, N., Poo, J., 1990. Coalescence and separation in binary collisions of droplets. J. Fluid Mech. 221, 183–204.

Aulisa, E., Manservisi, S., Scardovelli, R., Zaleski, S., 2007. Interface reconstruction with least-squares fit and split advection in three-dimensional cartesian geometry. Journal of Computational Physics 225 (2), 2301 – 2319. URL `http://www.sciencedirect.com/science/article/pii/S0021999107001325`

Bell, J. B., Colella, P., Glaz, H. M., 1989. A second-order projection method for the incompressible navier-stokes equations. Journal of Computational Physics 85 (2), 257–283.

Brackbill, J., Kothe, D. B., Zemach, C., 1992. A continuum method for modeling surface tension. Journal of computational physics 100 (2), 335–354.

Caboussat, A., Francois, M. M., Glowinski, R., Kothe, D. B., Sicilian, J. M., 2008. A numerical method for interface reconstruction of triple points within a volume tracking algorithm. Mathematical and Computer Modelling 48 (11), 1957–1971.

Chen, R.-H., Chen, C.-T., 2006. Collision between immiscible drops with large surface tension difference: diesel oil and water. Experiments in Fluids 41, 453–461.

Chen, X., Yang, V., 2014. Thickness-based adaptive mesh refinement methods for multi-phase flow simulations with thin regions. Journal of Computational Physics 269 (0), 22 – 39.
URL `http://www.sciencedirect.com/science/article/pii/S0021999114001612`

Chenadec, V. L., Pitsch, H., 2013. A 3d unsplit forward/backward volume-of-fluid approach and coupling to the level set method. Journal of Computational Physics 233 (0), 10 – 33.

Chorin, A. J., October 1968. Numerical solution of the Navier-Stokes equations. Journal of Computational Physics 22, 745–762.

Cossali, G., Coghe, A., Marengo, M., 1997. The impact of a single drop on a wetted solid surface. Experiments in fluids 22 (6), 463–472.

Desjardins, O., Moureau, V., Pitsch, H., 2008. An accurate conservative level set/ghost fluid method for simulating turbulent atomization. Journal of Computational Physics 227 (18), 8395–8416.

Duffy, A., Kuhnle, A., Sussman, M., 2012. An improved variable density pressure projection solver for adaptive meshes, unpublished. http://www.math.fsu.edu/s̃ussman/MGAMR.pdf.

Dyadechko, V., Shashkov, M., 2005. Moment-of-fluid interface reconstruction. Los Alamos report LA-UR-05-7571.

Dyadechko, V., Shashkov, M., 2008. Reconstruction of multi-material interfaces from moment data. Journal of Computational Physics 227 (11), 5361–5384.

Grant, R. P., Middleman, S., 1966. Newtonian jet stability. AIChE Journal 12 (4), 669–678.

Hirt, C. W., Nichols, B. D., 1981. Volume of fluid (vof) method for the dynamics of free boundaries. Journal of computational physics 39 (1), 201–225.

Jemison, M., Loch, E., Sussman, M., Shashkov, M., Arienti, M., Ohta, M., Wang, Y., 2013. A coupled level set-moment of fluid method for incompressible two-phase flows. Journal of Scientific Computing 54 (2-3), 454–491.

Jemison, M., Sussman, M., Arienti, M., 2014. Compressible, multiphase semi-implicit method with moment of fluid interface representation. Journal of Computational Physics 279, 182–217.

Jemison, M., Sussman, M., Shashkov, M., 2015. Filament capturing with the multimaterial moment-of-fluid method. Journal of Computational Physics.

Jiang, T.-S., Soo-Gun, O., Slattery, J. C., 1979. Correlation for dynamic contact angle. Journal of Colloid and Interface Science 69 (1), 74–77.

Kang, M., Fedkiw, R. P., Liu, X.-D., 2000. A boundary condition capturing method for multiphase incompressible flow. Journal of Scientific Computing 15 (3), 323–360.

Kim, H.-Y., Chun, J.-H., 2001. The recoiling of liquid droplets upon collision with solid surfaces. Physics of fluids 13, 643.

Kim, J., 2007. Phase field computations for ternary fluid flows. Computer methods in applied mechanics and engineering 196, 4779–4788.

Kucharik, M., Garimella, R. V., Schofield, S. P., Shashkov, M. J., 2010. A comparative study of interface reconstruction methods for multi-material ale simulations. Journal of Computational Physics 229 (7), 2432–2452.

Kwatra, N., Su, J., Grétarsson, J. T., Fedkiw, R., 2009. A method for avoiding the acoustic time step restriction in compressible flow. Journal of Computational Physics 228 (11), 4146–4161.

Li, X., Arienti, M., Soteriou, M. C., Sussman, M., 2010. Towards an efficient, high-fidelity methodology for liquid jet atomization computations. In: AIAA Aerospace Sciences Meeting.

Lin, S.-P., 2003. Breakup of liquid sheets and jets. Cambridge University Press New York.

Liovic, P., Rudman, M., Liow, J.-L., Lakehal, D., Kothe, D., 2006. A 3d unsplit-advection volume tracking algorithm with planarity-preserving interface reconstruction. Computers & fluids 35 (10), 1011–1032.

Ménard, T., Tanguy, S., Berlemont, A., 2007. Coupling level set/vof/ghost fluid methods: Validation and application to 3d simulation of the primary break-up of a liquid jet. International Journal of Multiphase Flow 33 (5), 510–524.

Nikolopoulos, N., Nikas, K.-S., Bergeles, G., 2009. A numerical investigation of central binary collision of droplets. Computers and Fluids 38 (6), 1191 – 1202.
URL `http://www.sciencedirect.com/science/article/pii/S0045793008002296`

Noel, E., Berlemont, A., Cousin, J., Menard, T., 2012. Application of the immersed boundary method to simulate flows inside and outside the nozzles. ICLASS 2012, 12th Triennial International Conference on Liquid Atomization and Spray Systems, Heidelberg, Germany, September 26.

Okawa, T., Shiraishi, T., Mori, T., 2006. Production of secondary drops during the single water drop impact onto a plane water surface. Experiments in fluids 41 (6), 965–974.

Orme, M., 1997. Experiments on droplet collisions, bounce, coalescence and disruption. Prog. Energy Combust. Sci. 23, 65–79.

Osher, S., Fedkiw, R. P., 2001. Level set methods: an overview and some recent results. Journal of Computational physics 169 (2), 463–502.

Osher, S., Sethian, J. A., 1988. Fronts propagating with curvature-dependent speed: algorithms based on hamilton-jacobi formulations. Journal of computational physics 79 (1), 12–49.

Palacios, J., Gómez, P., Zanzi, C., López, J., Hernández, J., 2010. Experimental study on the splash/deposition limit in drop impact onto solid surfaces. Proceedings of 23rd ILASS-2010, Brno, Czech Republic.

Pilliod Jr, J. E., Puckett, E. G., 2004. Second-order accurate volume-of-fluid algorithms for tracking material interfaces. Journal of Computational Physics 199 (2), 465–502.

Raessi, M., 2008. A level set based method for calculating flux densities in two-phase flows. Annual Research Briefs (Center for Turbulence Research, Stanford).

Raessi, M., Pitsch, H., 2009. Modeling interfacial flows characterized by large density ratios with the level set method. Annual Research Brief, Center for Turbulence Research.

Rayleigh, L., 1878. On the instability of jets. Proceedings of the London Mathematical Society, 4–13.

Rieber, M., Frohn, A., 1999. A numerical study on the mechanism of splashing. International Journal of Heat and Fluid Flow 20 (5), 455–461.

Rudman, M., 1998. A volume-tracking method for incompressible multifluid flows with large density variations. International Journal for Numerical Methods in Fluids 28 (2), 357–378.

Sallam, K., Aalburg, C., Faeth, G., 2004. Breakup of round nonturbulent liquid jets in gaseous crossflow. AIAA journal 42 (12), 2529–2540.

Sallam, K., Dai, Z., Faeth, G., 1999. Drop formation at the surface of plane turbulent liquid jets in still gases. International journal of multiphase flow 25 (6), 1161–1180.

Scardovelli, R., Zaleski, S., 2003. Interface reconstruction with least-square fit and split eulerian–lagrangian advection. International Journal for Numerical Methods in Fluids 41 (3), 251–274.

Schofield, S. P., Garimella, R. V., Francois, M. M., Loubere, R., 2008. Material order-independent interface reconstruction using power diagrams. International Journal for Numerical Methods in Fluids 56 (6), 643–659.
URL `http://dx.doi.org/10.1002/fld.1544`

Schofield, S. P., Garimella, R. V., Francois, M. M., Loubere, R., 2009. A second-order accurate material-order-independent interface reconstruction technique for multi-material flow simulations. Journal of Computational Physics 228 (3), 731 – 745.
URL `http://www.sciencedirect.com/science/article/pii/S0021999108005081`

Sijoy, C., Chaturvedi, S., 2010. Volume-of-fluid algorithm with different modified dynamic material ordering methods and their comparisons. Journal of Computational Physics 229 (10), 3848 – 3863.
URL `http://www.sciencedirect.com/science/article/pii/S0021999110000549`

Son, G., Hur, N., 2002. A coupled level set and volume-of-fluid method for the buoyancy-driven motion of fluid particles. Numerical Heat Transfer: Part B: Fundamentals 42 (6), 523–542.

Stewart, P., Lay, N., Sussman, M., Ohta, M., 2008. An improved sharp interface method for viscoelastic and viscous two-phase flows. Journal of Scientific Computing 35 (1), 43–61.

Sussman, M., 2003. A second order coupled level set and volume-of-fluid method for computing growth and collapse of vapor bubbles. Journal of Computational Physics 187 (1), 110–136.

Sussman, M., 2005. A parallelized, adaptive algorithm for multiphase flows in general geometries. Computers and Structures 83, 435–444.

Sussman, M., Almgren, A. S., Bell, J. B., Colella, P., Howell, L. H., Welcome, M. L., 1999. An adaptive level set approach for incompressible two-phase flows. Journal of Computational Physics 148 (1), 81–124.

Sussman, M., Fatemi, E., Smereka, P., Osher, S., 1998. An improved level set method for incompressible two-phase flows. Computers & Fluids 27 (5), 663–680.

Sussman, M., Ohta, M., 2009. A stable and efficient method for treating surface tension in incompressible two-phase flow. SIAM J. Sci. Comput. 31 (4), 2447–2471.

Sussman, M., Puckett, E. G., 2000. A coupled level set and volume-of-fluid method for computing 3d and axisymmetric incompressible two-phase flows. Journal of Computational Physics 162 (2), 301–337.

Sussman, M., Smereka, P., Osher, S., 1994. A level set approach for computing solutions to incompressible two-phase flow. Department of Mathematics, University of California, Los Angeles.

Tanguy, S., Berlemont, A., 2005. Application of a level set method for simulation of droplet collisions. International Journal of Multiphase Flow 31 (9), 1015 – 1035.
URL `http://www.sciencedirect.com/science/article/pii/S0301932205000832`

Taylor, G., 1963. Generation of ripples by wind blowing over viscous fluid. The Scientific Papers of GI Taylor, 244–254.

Wang, Y., Simakhina, S., Sussman, M., 2012. A hybrid level set-volume constraint method for incompressible two-phase flow. Journal of Computational Physics.

Wang, Z., Yang, J., Koo, B., Stern, F., 2009. A coupled level set and volume-of-fluid method for sharp interface simulation of plunging breaking waves. International Journal of Multiphase Flow 35 (3), 227–246.

Weymouth, G., Yue, D. K.-P., 2010. Conservative volume-of-fluid method for free-surface simulations on cartesian-grids. Journal of Computational Physics 229 (8), 2853–2865.

Yarin, A., 2006. Drop impact dynamics: splashing, spreading, receding, bouncing. Annu. Rev. Fluid Mech. 38, 159–192.